HHS Public Access

Author manuscript

Dev Cell. Author manuscript; available in PMC 2023 February 07.

Published in final edited form as:

Dev Cell. 2022 February 07; 57(3): 310–328.e9. doi:10.1016/j.devcel.2022.01.006.

Epigenetic basis of oncogenic-*Kras* mediated epithelial-cellular proliferation and plasticity

Preetish Kadur Lakshminarasimha Murthy[1,2,3,16,*], **Rui Xi**[1,4,16], **Diana Arguijo**[1], **Jeffrey I. Everitt**[5], **Dewran D. Kocak**[1,4], **Yoshihiko Kobayashi**[3], **Aline Bozec**[6], **Silvestre Vicent**[7,8,9,10], **Shengli Ding**[1,4,11], **Gregory E. Crawford**[4,11,12], **David Hsu**[13], **Purushothama Rao Tata**[3,11], **Timothy Reddy**[4,11,14], **Xiling Shen**[1,4,11,15,17,*]

[1.] Department of Biomedical Engineering, Duke University, Durham, NC 27708, USA

[2.] Sibley School of Mechanical and Aerospace Engineering, Cornell University, NY 14853, USA

[3.] Department of Cell Biology, Duke University Medical Center, Durham, NC 27710, USA

[4.] Center for Genomics and Computational Biology, Duke University, Durham, NC 27708, USA

[5.] Department of Pathology, Duke University Medical Center, Durham, NC 27710, USA

[6.] Friedrich-Alexander-University Erlangen-Nürnberg (FAU), Department of Internal Medicine 3 – Rheumatology and Immunology, Universitätsklinikum Erlangen, Erlangen, Germany

[7.] University of Navarra, Center for Applied Medical Research, Program in Solid Tumors, Pamplona, SPAIN.

[8.] University of Navarra, Department of Pathology, Anatomy and Physiology, Pamplona, Spain

[9.] IdiSNA, Navarra Institute for Health Research, Pamplona, Spain

[10.] Centro de Investigación Biomédica en Red de Cáncer (CIBERONC), Madrid, Spain

[11.] Center for Advanced Genomic Technologies, Duke University, Durham, NC 27708, USA

[12.] Department of Pediatrics, Division of Medical Genetics, Duke University, Durham, NC 27710, USA

[*]Correspondence: P.K.L.M. (pk434@cornell.edu) and X.S. (xiling.shen@duke.edu).

AUTHOR CONTRIBUTIONS

PKLM and XS initiated the study. PKLM and RX designed and performed all the experiments, unless stated otherwise, and interpreted the data. PKLM and DA performed bioinformatic analysis. PKLM and JE performed histopathological assessment of tissue sections. DA quantified the spheroid size and number in tumour initiation assay. RX performed quantification of IF experiments. DH generated the PDX model. AB provided *Fosl1*$^{fl/fl}$ mice. SV provided KP cell line. DK and TR provided the FOSL1-Flag tagged A549 cell line. YK and PRT assisted with scRNA-seq and Mnt-ChIP library preparation. GEC assisted in interpreting ATAC-seq data. PKLM wrote the manuscript with inputs from RX, DA and XS. XS secured funding. All authors reviewed the manuscript.

DECLARATION OF INTERESTS

X.S. is the co-founder and CEO of Xilis, Inc, a company that develops droplet organoids for clinical diagnostics. This study does not overlap with Xilis' commercial interests. P.R.T. serves as a consultant for Surrozen Inc., Cellarity Inc., and Celldom Inc., on work not related to the contents of this manuscript.

INCLUSION AND DIVERSITY

One or more of the authors of this paper self-identifies as an underrepresented ethnic minority in science. One or more of the authors of this paper received support from a program designed to increase minority representation in science.

[13] Department of Medicine, Duke University Medical Center, Durham, NC 27710, USA

[14] Department of Biostatistics and Bioinformatics, Duke University Medical Center, Durham, NC 27710, USA

[15] Terasaki Institute for Biomedical Innovation, Los Angeles, CA 90024, USA

[16] These authors contributed equally

[17] Lead contact.

SUMMARY

Oncogenic *Kras* induces a hyper-proliferative state that permits cells to progress to neoplasms in diverse epithelial tissues. Depending on the cell-of-origin, this also involves lineage transformation. Although a multitude of downstream factors have been implicated in these processes, the precise chronology of molecular events controlling them remains elusive. Using mouse models, primary human tissues and cell lines, we show that, in *Kras*-mutant alveolar type II cells (AEC2), FOSL1-based AP-1 factor guides mSWI/SNF complex to increase chromatin accessibility at genomic loci controlling the expression of genes necessary for neoplastic transformation. We identified two orthogonal processes in *Kras*-mutant distal airway club cells. The first promoted their transdifferentiation into an AEC2-like state through NKX2.1 and the second controlled oncogenic transformation through the AP-1 complex. Our results suggest neoplasms retain an epigenetic memory of their cell-of-origin through cell-type specific transcription factors. Our analysis showed that a cross-tissue conserved AP-1-dependent chromatin remodelling program regulates carcinogenesis.

eTOC

Murthy, Xi et al., study the epigenetic reprogramming caused by mutant-Kras in pulmonary AEC2 and club, as well as intestinal *Lgr5*$^{+}$ stem cells. They identify an AP-1 driven transformation program conserved across tissues and that tumor cells retain an epigenetic memory of their cell-of-origin through cell-type specific transcription factors.

Graphical Abstract

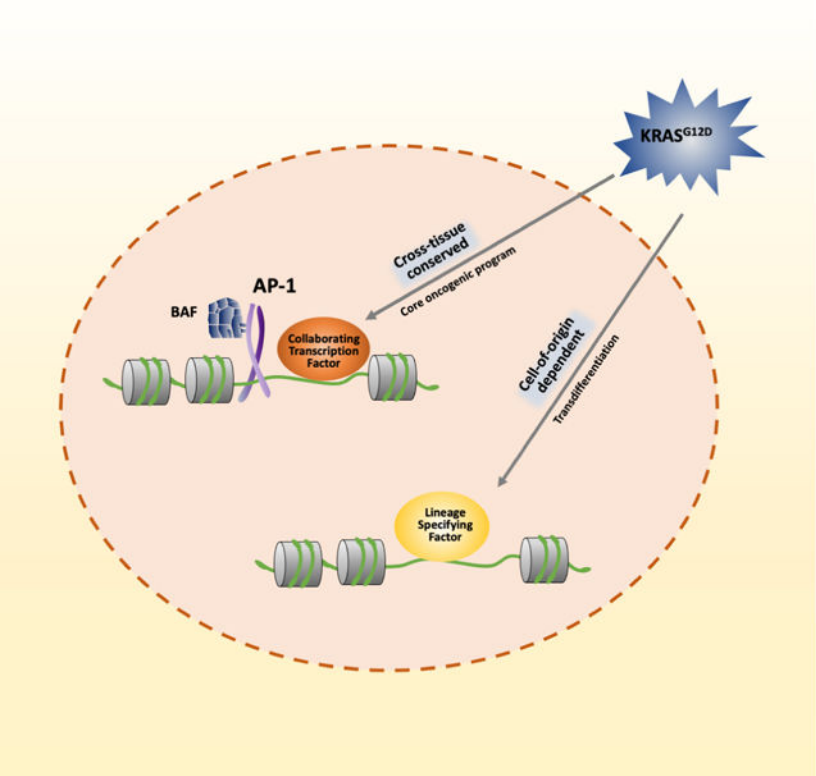

INTRODUCTION

Mutant KRAS, one of the most frequent drivers of epithelial cancers, is found in approximately 97% of pancreatic ductal adenocarcinomas (PDAC), 45% of colorectal adenocarcinomas (COAD) and 30% of lung adenocarcinomas (LUAD) (Cox et al., 2014). Oncogenic mutation keeps KRAS in its active GTP-bound state leading to constant downstream signalling through RAF, PI3K and other kinases leading to uncontrolled cellular proliferation (Pylayeva-Gupta et al., 2011). Research over the years has shown that the role of mutant KRAS in neoplasia involves not only the self-sufficiency of growth factors but other 'hallmarks of cancer' as well (Hanahan and Weinberg, 2000; Pylayeva-Gupta et al., 2011). KRAS-mutant cells that undergo transformation are able to suppress apoptosis, reprogram their metabolism, remodel their microenvironment by inducing angiogenesis and evade an immune response (Pylayeva-Gupta et al., 2011). However, it has also been shown that in many primary cell types with unmutated P53 and $P16^{Ink4a}$ - $P19^{Arf}$ pathways, expression of mutant *Kras* leads to a senescent phenotype (Junttila et al., 2010; Kamijo et al., 1997; Sarkisian et al., 2007; Serrano et al., 1997). And there are reports of colonic epithelial cells that are seemingly unaffected by mutant KRAS (Aivado et al., 2000; Zhu et al., 1997). These suggest that the ability of mutant *Kras* depends on how pliable a cell is to be transformed into a neoplastic one.

Cellular identity which, for a long time, was defined by the expression of a handful, if not one, of marker genes, is now - with the advent of single-cell transcriptomics - being defined by the overall mRNA composition (Shapiro et al., 2013). However, recent studies

have shown how the organisation of chromatin affects the function of transcription factors and the need to include epigenetic information to define cellular identity (Bell et al., 2011; Buenrostro et al., 2018; Chen et al., 2019; Morris, 2019). This made us consider whether the chromatin organisation in a cell is a determinant of its response to oncogenic KRAS. More importantly, if a drastic remodelling of chromatin is critical for KRAS driven neoplastic transformation (Ge et al., 2017).

Adult epithelial cells can often be scored based on their stemness, that is the ability to self-renew and differentiate into other cell types, and categorised into stem, progenitor and differentiated cells (Rawlins and Hogan, 2006). Resident stem cells have been shown to be the origin of tumours in their respective tissues (Barker et al., 2009; Latil et al., 2017). However, many cell types and sub-types have been shown to demonstrate stemness in the lung (Barkauskas et al., 2013; Kumar et al., 2011; Nabhan et al., 2018; Zacharias et al., 2018). Cells in the pulmonary epithelial lining also show remarkable plasticity (Tata and Rajagopal, 2017). The two main cell types of the alveolus, alveolar type I (AEC1) and alveolar type II (AEC2), can give rise to each other under appropriate conditions (Barkauskas et al., 2013; Jain et al., 2015). Club and basal cells of the airway show a similar behaviour (Tata and Rajagopal, 2017). Ciliated cells of the airway have been shown to transdifferentiate into goblet cells (Avila, 2011; Turner et al., 2011). Accordingly, many cell types have been purported to be cell of origin of lung tumours (Sutherland et al., 2014). Hence, the pulmonary epithelium is a good system to study the effect of mutant *Kras* in various cell types and follow changes to the chromatin architecture in each case.

In this study we have used mouse models to characterise the changes to the accessible chromatin during the initial stages of $Kras^{G12D}$ driven tumorigenesis in AEC2 and club cells of the lung, where we found an AP-1 dependent increase in accessibility. Significantly, we found that oncogenic *Kras* activity in epithelia of diverse organs including lung, skin and intestine also follows a similar trajectory. Therefore, our study implicates a conserved pathway to target *Kras*-driven tumours.

RESULTS

AP-1 mediates an epigenome-wide increase in nucleosome occupancy in $Kras^{G12D}$ mutant alveolar cells

Intranasal delivery of a viral vector containing Cre-recombinase to $Kras^{LSL\text{-}G12D/+}$; $Trp53^{fl/fl}$ mice is one of the most common methods used to model lung adenocarcinoma (Jackson et al., 2005; Junttila et al., 2010; Kwon and Berns, 2013; Tammela et al., 2017; Vallejo et al., 2017; Winslow et al., 2011). However, as mutant *Kras* is expressed in multiple cell types in this model, we chose the methods described by Xu and colleagues (Xu et al., 2012), where Cre recombinase is expressed in a cell-type specific manner. Unlike (Xu et al., 2012), tumour suppressor *Trp53* was not deleted in our study as it has been shown to be non-essential during the early stages of lung tumorigenesis (Muzumdar et al., 2016). This allows us to delineate, specifically, the effects of mutant *Kras* in pulmonary tumours.

We studied the initial stages of KRAS-mediated lung carcinogenesis using the *Sftpc*-CreER; $Kras^{LSL\text{-}G12D/+}$; *R26R*-tdTomato mouse line, henceforth referred to as SK model (Figure

1A). Here, mutant *Kras* is expressed by the alveolar type II (AEC2) cells after tamoxifen doses leading to their proliferation (Xu et al., 2012). Lungs were analysed at two- and four-weeks post Cre induction when hyperplastic lesions were found throughout the lung (Figures 1B). Several atypical adenomatous hyperplastic (AAH) lesions, adenomas and very rarely adenocarcinoma could also be observed (Figure S1A). Significant macrophage infiltration was seen in the hyperplastic regions likely due to the overproduction of surfactants by the proliferating type II cells (Wright, 1990) (Figures 1B and S1A). Area of the lung covered by various lesions was quantified (Figures S1B and S1C).

For further analysis, we isolated, by FACS, normal AEC2 cells from *Sftpc*-CreER; *R26R*-tdTomato mice (henceforth referred to as SC mice) and AEC2-derived neoplastic cells from SK mice based on the tdTomato label (Figures S1D–F). We performed the assay of transposase-accessible chromatin using sequencing, or ATAC-seq (Buenrostro et al., 2013), on isolated normal and neoplastic cells to identify changes to the chromatin state. We ensured that the data were reproducible (Figure S1G and S1H; Table S1). Principal component analysis (PCA) showed that the normal and neoplastic cells cluster separately indicating that they are in distinct epigenetic states (Figure 1C). We identified differentially accessible regions using DiffBind (Ross-Innes et al., 2012) (Figures 1D). Following the convention used by Denny and colleagues (Denny et al., 2016), we shall henceforth refer to the regions with increased accessibility in neoplastic cells as “newly open” regions and those with reduced accessibility in neoplastic cells as “newly closed”. We find that most of the differentially accessible regions are away from the Transcription Start Sites (TSS) and are in intronic or intragenic regions of the genome (putative *cis*-regulatory elements or enhancers) (Figures S1I and S1J). To understand their relevance to gene regulation, using GREAT, we mapped the newly open regions in the neoplastic cells to the genes whose expression they are likely to regulate (McLean et al., 2010). The gene set thus obtained strongly correlated with the genes upregulated in the Kras2LA lung adenocarcinoma model (Sweet-Cordero et al., 2005). Interestingly, the newly open regions also appear to regulate apoptotic pathway genes (Figure S1K).

To delineate the factors responsible for the epigenetic changes observed, we identified the transcription factor (TF) motifs enriched in the differentially accessible regions using HOMER (Heinz et al., 2010). In the AEC2 derived neoplastic cells, regions with increased accessibility are enriched for AP-1 motif sites and those with reduced accessibility harbour ETS and FOX family motifs (Figures 1E, 1F, SL–N; Table S2). Using PIQ (Protein Interaction Quantification), a machine-learning tool to identify binding probabilities of TFs, we found that AP-1 factors are more likely to be bound to the genome in *Kras* mutant cells than in normal AEC2 (Sherwood et al., 2014a) (Figure S2A). We then performed bivariate genomic footprinting using the BaGFoot algorithm which identifies differential TF activity based on changes to the TF footprint and TF motif flanking accessibility (Baek et al., 2017). AP-1 TFs showed significantly higher accessibility and deeper footprints in the neoplastic cells than in AEC2 cells, suggesting their increased activity (Figures 1G and 1H). These data raise the possibility that AP-1 is involved in increasing accessibility at the appropriate regions of chromatin to transform normal cells into neoplastic ones.

Transcription factors can displace nucleosomes to increase accessibility to genomic sites (Bell et al., 2011; Denny et al., 2016). To understand whether the AP-1 complex is involved in nucleosome remodelling, we evaluate changes to nucleosome occupancy at AP-1 motif occurrences in the newly accessible regions in neoplastic cells using NucleoATAC software (Schep et al., 2015). We find that in newly open regions in neoplastic cells, nucleosomes have been depleted at putative AP-1 binding sites, whereas no such change is observed in the constitutively open regions (Figure 1I). To ensure that the observation is specific to AP-1 and not newly open peaks, we perform a similar analysis at CTCF, a TF which was not identified as an outlier by BaGFoot analysis, motif occurrences. We found that nucleosome occupancy at CTCF motif occurrences in both AEC2 and SK neoplastic cells is nearly identical in the newly open regions (Figure 1I). We hypothesised that, if AP-1 were to be actively involved in increasing accessibility, a greater reduction of nucleosome occupancy at AP-1 motif centre with an increase in accessibility (i.e. fold change of the peak) should be seen. Indeed, we observed that the reduction in nucleosome occupancy at the AP-1, but not the CTCF, motif centre in newly open regions correlates with the fold change of newly open regions (Figure S2B).

We then sought to determine if similar results could be seen in *Kras*-mutant lung tumours when additional mutations such as loss of tumour-suppressor P53, reminiscent of human lung adenocarcinoma, are present. Tumours from KP mouse model in which intranasal delivery of adenoviral Cre-recombinase to $Kras^{LSL\text{-}G12D/+}$; $Trp53^{fl/fl}$ mice have been shown to resemble human lung adenocarcinoma (Jackson et al., 2005). We performed ATAC-seq on two KP tumour cell-lines. Similar to our observations with the SK model, newly open regions in KP tumour cells showed significant enrichment for AP-1 motifs (Figure S3A). The newly closed regions were enriched for NKX2.1, CEBP and FOXA1 motifs (Figure S3B). BaGFoot analysis further showed that AP-1 TF motifs had the highest change in flanking accessibility and footprint depth in KP tumours when compared to normal AEC2 cells (Figure S3C).

Next, we sought to determine if fully formed human tumours retain an increased accessibility at AP-1 motif sites. We isolated normal epithelial cells ($EpCAM^+$) from human lungs by FACS (Figure S2C). We xenografted a $KRAS^{G12D}$ mutant primary human lung adenocarcinoma sample in mice and collected the $EpCAM^+$ cells by FACS (Figures 1J, S2D and S2E). We performed ATAC-seq on these samples and analysed them along with published data of A549, a KRAS mutant lung adenocarcinoma cell line (Consortium, 2012). Both the normal and tumour cells have distinct chromatin accessibility profiles (Figures 1K and S2F). Newly open regions, akin to the mouse model, are enriched for AP-1 motifs (Figure 1L; Table S2). And the newly closed regions are strongly enriched for the NKX2.1 motif along with that of the FOX family factors similar to what was observed in the KP model (Figure S2G; Table S2). A549 cells are negative for NKX2.1 expression, but the PDX (patient derived xenograft), which was generated from a poorly differentiated tumour, cells expressed NKX2.1 (Figures 1J and S2H) (Maeda et al., 2012; Winslow et al., 2011). These data, along the results from KP tumours, point towards additional mutations affecting NKX2.1 activity in lung adenocarcinoma cells. Additionally, we re-analysed ATAC-seq data on TCGA samples (Corces et al., 2018). We found that in KRAS-mutant

lung adenocarcinoma (LUAD), AP-1 factors have the highest flanking accessibility when compared to that of other transcription factors in the open chromatin regions (Figure S2I).

Pharmacological inhibition of AP-1 reduces proliferation of *Kras*-mutant AEC2 cells *in vitro* and *in vivo*

To test whether AP-1 mediated changes to the open chromatin are necessary for tumour initiation, we performed an organoid based tumour initiation assay where mutant *Kras* is expressed in AEC2 cells seeded in Matrigel and their ability to form tumour spheroids is assayed under various conditions (Figure S2J). We validated the use of LysoTracker dye to isolate normal AEC2 cells without a genetic label (Figure S2K) (der Velden et al., 2013). We isolated normal AEC2 cells from *Sftpc*-CreER; LSL-*Kras*^{G12D}; R26R-tdTomato mice by sorting for the LysoTracker^{+} tdTomato^{-} population and excluded a small population of LysoTracker^{+} tdTomato^{+} cells that were present due to the activation of CreER in the absence of tamoxifen (Figure S2L). Normal AEC2 were plated and treated with 4-Hydroxytamoxifen (4-OHT) to express mutant *Kras* and simultaneously AP-1 activity was inhibited by a small molecule SR 11302 (Fanjul et al., 1994; Huang et al., 1997). After 8 days we observed that *Kras* mutant AEC2 cells form significantly smaller and fewer spheroids when AP-1 activity was inhibited in comparison to those treated by DMSO as control (Figures 2A and 2B).

AP-1 has been shown to control cell proliferation and apoptosis in a context dependent manner (Shaulian and Karin, 2001). To ensure that blockage of AP-1 activity is specifically affecting *Kras* mutant AEC2, we treated normal AEC2 from *Sftpc*-CreER; R26R-tdTomato mice with SR 11302 or DMSO (vehicle control) for 8 days. Blocking AP-1 activity does not significantly affect the number or size of normal AEC2 derived organoids (Figures 2C and 2D).

We further validate this observation by using a second AP-1 inhibitor T-5224 (Makino et al., 2017). We found that T-5224 treated *Kras*-mutant AEC2 cells form significantly smaller and fewer spheroids when compared to those treated with DMSO as control (Figures 2E and 2F). T-5224 treatment did not significantly affect the number or size of normal AEC2 derived organoids (Figures 2G and 2H).

To test the effect of AP-1 inhibitor on cancer cells that do not harbour KRAS mutations, we used three colon cancer cell lines. ATAC-seq for patient-derived normal colon organoids, HT29 cells, and patient-derived xenograft lines (CRC57 and CRC12x) were obtained from previous publications (Allen et al., 2019; Devall et al., 2020; Wang et al., 2021). BaGFoot analysis did not show AP-1 enrichment in any of the tumour cell lines when compared to the control, suggesting the absence of epigenome-wide chromatin remodelling by AP-1 factors in these cell lines (Figure S3E). Cells were cultured in matrigel for 5 days with or without the presence of SR 11302. We found that treatment of AP-1 inhibitor did not affect the proliferation or survival of these cells (Figure S3F).

To investigate whether blocking AP-1 activity would affect the *Kras*-mutant AEC2 cells *in vivo*, we injected SR 11302 or DMSO to SK mice along with tamoxifen doses and continued to administer the drug or vehicle control for 3 weeks (Figure 2I). *Kras* mutant AEC2 cells

from the lungs of mice that received the AP-1 inhibitor showed an almost 3-fold reduction in proliferation (Figures 2J and 2K).

FOSL1 based AP-1 complex recruits mSWI/SNF to displace nucleosomes in *Kras*-mutant cells

AP-1 complex consists of various combinations of dimers of FOS (FOS, FOSB, FOSL1 and FOSL2) and JUN (JUN, JUNB and JUND) family proteins, all of which have a similar DNA binding motif, making them difficult to distinguish bioinformatically (Eferl and Wagner, 2003; Khan et al., 2017; Vierbuchen et al., 2017). We performed RNA-seq of AEC2 and neoplastic cells to see if changes in gene expression could offer clues to identify the AP-1 complex composition (Figures S4A–C). We find that only *Fosl1*, among the *Fos* and *Jun* family genes, is upregulated in *Kras* mutant neoplastic cells (Figure 3A). We also observed increased FOSL1 protein levels in the neoplastic lungs when compared to normal (Figure 3B and 3C). This is consistent with recent publications showing that *Fosl1* is important in *Kras* driven lung adenocarcinomas and its expression is inversely correlated with patient survival (Elangovan et al., 2018; Vallejo et al., 2017).

Heterodimers of FOS and JUN family proteins have been shown to open the chromatin at enhancer loci by recruiting mammalian SWI/SNF or BAF complex and aid in the differentiation of mouse embryonic fibroblasts (MEFs) (Vierbuchen et al., 2017). Interaction of SWI/SNF complex with AP-1 factors has also been shown in human colorectal, adrenal and hepatic tumours (Ito et al., 2001; Kelso et al., 2017; Nakatsuka et al., 2017). Similarly, we hypothesised that AP-1 complex consisting of FOSL1 is involved in chromatin remodelling and directing the development of mutant-*Kras* driven tumours.

We used A549, a KRAS mutant human lung adenocarcinoma cell line, cells in which FOSL1 was FLAG tagged. We extracted nuclear protein from these cells and immunoprecipitated (IP) the FLAG-tagged protein while using the extract from WT A549 cells as a control (Figure 3D). We used mass spectrometry to identify proteins that co-precipitated with FOSL1. Known binding-partners of FOSL1, JUNB, JUN and JUND were detected (Eferl and Wagner, 2003). We also detected SWI/SNF complex proteins SMARCC2, ACTL6A etc. confirming that AP-1 directly binds to the nucleosome remodelling BAF complex in KRAS mutant cells (Figure 3E).

To test the role of FOSL1 in mediating the changes to the accessible chromatin in *Kras* mutant cells, we crossed SK mice with *Fosl1*$^{fl/fl}$ mice (SFK model) (Eferl et al., 2004). After Cre mediated recombination, exons 3 and 4 of *Fosl1* gene are deleted and FOSL1-GFP reporter is expressed in these mice (Eferl et al., 2004). Based on the data described in the previous section and in literature (Elangovan et al., 2018) where FOSL1 was shown to repress apoptosis in KRAS-mutant human lung adenocarcinoma cells, we hypothesised that *Kras*-mutant AEC2 cells with homozygous deletion of *Fosl1* would either apoptose or be outcompeted by those with heterozygous or no deletion (owing to incomplete Cre-recombinase activity). 4 weeks after tamoxifen doses to *Sftpc*-CreER; *Kras*$^{LSL-G12D/+}$; *Fosl1*$^{fl/fl}$; *R26R*-tdTomato mice we observed that only about 1% of lineage labelled (tdTomato^{+}) cells expressed GFP at detectable levels (Figures 3F and 3G). We confirmed that tdTomato^{+} GFP^{+} cells express high levels of *Fosl1* by RT-qPCR using primers specific

to the intact *Fosl1* transcript (Figure S4D). We performed ATAC-seq on sorted tdTomato$^+$ GFP$^+$ cells and found reads that mapped to exons 3 and 4 of the *Fosl1* gene confirming that Cre mediated recombination was incomplete and only one allele of *Fosl1* had been deleted and replaced by GFP in these cells (Figure S4E). These data suggest that tdTomato$^+$ GFP$^+$ cells have the highest *Fosl1* expression among the labelled cells. BagFoot analysis showed that tdTomato$^+$ GFP$^+$ cells have a significantly higher flanking accessibility at the AP-1 motif when compared to AEC2 cells and SK 4w neoplastic cells (Figures 3H and I). These observations suggest that increasing *Fosl1* expression leads to an increase in AP-1 signature on the chromatin.

To confirm that Fosl1 binds to the newly accessible chromatin regions, we performed ChIP-seq on SK neoplastic cells and KP tumour cell-lines using the Mnt-ChIP protocol (van Galen et al., 2016). We observed that FOSL1 binding pattern closely resembled that of accessible chromatin. FOSL1 ChIP-seq peaks were detected at the open chromatin regions of SK neoplastic cells (Figure 3J and S4F). Quantification showed that almost 41% of the newly open peaks in SK tumours had a FOSL1 binding site contrary to less than 10% of the newly closed regions (Figure 3K). Collectively, these observations suggest that FOSL1 mSWI/SNF factors to displace nucleosomes and increase accessibility at genomic loci regulating tumour growth.

De-multiplexing cellular plasticity and proliferative signal in club cell origin tumours

Cell of origin of human lung adenocarcinoma has remained elusive (Rowbotham and Kim, 2014). Observation of ultrastructural features like that of AEC2 in human lung tumours and detection of surfactants, especially surfactant protein C, in murine models had alluded to AEC2 cell being their originator (Adamson et al., 1969; Coalson et al., 1970; Desai et al., 2014; Jackson et al., 2001). However, many other studies on human and murine lung tumours have suggested that they arise from club cells (Dermer, 1981; Rowbotham and Kim, 2014; Spella et al., 2019). We tried to understand the changes to the accessible chromatin in club cells upon *Kras* mutation using the mouse line: *Scgb1a1*-CreER; *Kras*$^{LSL\text{-}G12D/+}$; R26R-fGFP, henceforth referred to as CK model. Lungs were analysed 4, 10, 16- and 22-weeks post Cre-recombinase induction (Figure 4A). Neoplastic transformation is slower here when compared to the SK model (Figures 1B and 4B). Terminal bronchiolar hypertrophy is mostly observed 4 weeks post the tamoxifen doses. Alveoli appear largely normal at this stage. Bronchiolar hyperplasia was observed after 10 weeks, while adenomas and adenocarcinomas were found after 16 weeks. Lesions appeared to arise from the bronchioles and protruded into the alveolar space (Figure 4B). Areas occupied by these lesions were quantified and summarised in Figures S5A and S5B. Lineage labelled cells in the alveolar regions around terminal bronchioles expressed SOX2, suggesting their airway origin (Figure S5C).

In this model, although CreER induction is mainly seen in club cells, a small fraction (~1%) of AEC2 (CC10$^+$ AEC2) and putative bronchioalveolar stem cells (BASCs) also show CreER activity after tamoxifen doses (Rawlins et al., 2009; Xu et al., 2012). A pure population of normal club cells was isolated from *Scgb1a1*-CreER; R26R-fGFP mice (henceforth referred to as CC mice) by a combination of fGFP label and LysoTracker dye

staining (Figures S5D, and S5E). Neoplastic cells from CK mice were isolated by FACS using the lineage label fGFP (Figure S5F). Additionally, visible tumours (larger than ~2 mm in diameter) were excised from CK 22w lungs, dissociated and fGFP labelled cells were isolated for further analysis. We performed ATAC-seq on the normal and neoplastic cells collected at various stages (Figure S5G). Disease progression can be visualised by PCA (Figure 4C). CK 22w lungs have higher heterogeneity among their lesions when compared to other stages. There is also a high variation in the number of adenomas found at this stage (Figure S5B). Hence a lower correlation between the replicates at 22w time-point was observed. We identified differentially accessible regions in various stages of tumorigenesis using DiffBind (Figures S5H and S5I) (Ross-Innes et al., 2012).

Similar to our observation in the SK model, newly open regions are mainly found away from transcription start sites and are in intronic or intragenic regions of the genome (Figures S5I and S5J). We found that the newly open regions in neoplastic cells, collected at all the stages, are enriched for AP-1 motifs (Figures S6A and S6B; Table S2). *Fosl1* transcript level showed a four-fold increase in CK 22w neoplastic cells when compared to the club cells (Figure S6C). FOSL1 protein was detected in neoplastic cells at various stages of tumorigenesis (Figures 4D, 4E, S6D and S6E). We performed BaGFoot analysis and observed a progressive increase in flanking accessibility at AP-1 motif occurrences (Figures 4F, 4G and S6F–J). A linear increase was observed with time in the ratio of percentage of sites harbouring an AP-1 motif in the newly open regions to that in background sequences (Figure S6K). There was a reduction in the nucleosome occupancy at the AP-1 motif centre in the newly open peaks (Figures S6L and S6M). These observations in both SK and CK models point to a conserved mechanism by which mutant KRAS remodels the epigenetic landscape and transforms pulmonary epithelial cells.

CK model provides us with the advantage of tracking the epigenetic changes with tumour development. By hierarchical clustering we identified three classes of differentially accessible regions (Figure 4H). The first among them encompassed regions that have high accessibility in Club cells but low in all four neoplastic stages. Motif sites of FOX family TFs were enriched here. The second cluster had regions that gradually increase in accessibility with time and was strongly enriched for AP-1 motif sites in concurrence with the BaGFoot analysis (Figures 4F and 4H). An example is shown at the *Ccnd1* locus (Figure 4I).

The third cluster in Figure 4H consisted of regions with low accessibility in the club cells but high in all the neoplastic stages. Lung epithelial lineage specific transcription factor, NKX2.1, had its motif sites enriched here. NKX2.1 expression was detected in neoplastic cells (Figure 4J). Ontology analysis, using GREAT, of the regions in this cluster harbouring an NKX2.1 motif shows that they are involved in concomitant AEC2-cell functions such as the production of lysozyme and surfactants (Figure 4K). SPC was expressed by lineage-labelled ($fGFP^+$) cells at early and late stages of tumorigenesis (Figures 4L, S6N). This is consistent with previous reports where SPC has been detected in club cell derived neoplastic cells (Spella et al., 2019; Xu et al., 2012). These data suggest that mutant KRAS signalling transdifferentiates club cells to an AEC2-like state through NKX2.1 activity.

To further characterise this, we performed scRNA-seq using Drop-seq protocol (Macosko et al., 2015). We injected four doses of tamoxifen to six control (CC) mice and harvested the lungs after two weeks. The lungs were dissociated into single cells and immune and endothelial cells were depleted by MACS. We further enriched for lineage labelled ($fGFP^+$) cells by FACS. $fGFP^+$ cells and immune and endothelial depleted total lung cells were mixed in equal number before droplet-generation for scRNA-seq to get adequate representation of multiple of the populations of interest. To characterise the neoplastic cells. We injected four doses of tamoxifen to 2 CK mice and harvested the lungs after 6 weeks. We purified lineage labelled ($fGFP^+$) cells by FACS. We spiked in immune and endothelial depleted total lung cells so that they formed 20% of total cells used for droplet-generation. We identified AEC2, club, mucous and ciliated cells among the epithelial cells from control lungs and corresponding AEC2-like, club-like and ciliated cells from CK lungs (Figures 5A–E). AEC2-like cells could further be categorised into three types. AEC2-like-1 was the closest in its transcriptional state to normal AEC2 cells and expressed high levels of canonical markers *Sftpc*, *Lamp3* and *Napsa*. AEC2-like-2 population was enriched for c-Myc targets *Gadd45a*, *Ddit3* and *Foxo3*. AEC2-like-3 cells, interestingly, showed the expression of *Nfkbia* which has been implicated in Cisplatin resistance (Heavey et al., 2014) and transcription factor *Klf4* which is known regulate lung tumour initiating cells (Yu et al., 2016) (Figure 5F). Additionally, we found pre-AEC1 (PATS)-like cells, expressing *Sfn*, *Cldn4* and *Lgals3*, and enriched for P53-pathway, in CK lungs (Figure 5B, E and G).

We compared the club-like cells from CK mice to normal club cells and found that “surfactant metabolism” pathway was strongly enriched in them (Figure 5H). This is consistent with our observation from ATAC-seq in Figure 4K. We further perform RNA velocity analysis in which the ratio of unspliced and spliced mRNA variants are used to estimate the trajectories cell-states (La Manno et al., 2018) (Figure 5I). These data suggest that club-like neoplastic cells eventually turn into AEC2-like cells.

To further validate this observation, we used an *in vitro* organoid system. We injected four doses of tamoxifen to CK mice and harvested lungs after 2 days. $Lysotracker^-$ $fGFP^+$ cells were isolated by FACS and plated with MRC5 fibroblasts in Matrigel. The cells were cultured for ten days before fixation (Figure 5J). Immunostaining showed that an average of 35% of cells expressed AEC2 marker SFTPC (Figures 5K and L). Taken together, these data suggest that mutation of *Kras* in club cells generates tumour cells with alveolar characteristics.

Cell of origin influences the neoplastic cell state

AP-1 has been shown to select enhancer loci while cooperating with cell type specific transcription factors (Vierbuchen et al., 2017). We observed that, out of 3,655 newly open regions that harbour an AP-1 motif in SK 4w neoplastic cells, 1,689 (46%) are also newly open in the CK 22w neoplastic cells (Figure 6A). CK 22w also has another 9,029 regions containing an AP-1 motif specific to them. (Figure 6A). We used Centrimo package to identify TF motifs enriched in the neighbourhood (~50 bp away) of putative AP-1 binding sites in regions open only in SK 4w cells or CK 22w neoplastic cells, and the overlapping regions (Bailey et al., 2009). We rank ordered the enriched TF motifs in each of the three

cases based on adjusted P-value and summarised the top hits in a “bubble-plot” (Figure 6A; Table S3). We hypothesised that the factor ranked high in CK specific peaks and low in the other two cases could be a CK specific collaborating TF. We identify HES1, TF downstream of Notch signalling, as one such factor (Figure 6A). A similar analysis on putative AP-1 binding sites in regions open only in SK 4w cells or CK 16w neoplastic cells, and the overlapping regions also identifies HES1 as a collaborating factor specific to club cell origin tumours (Figure 6B; Table S4). Detection of cleaved Notch1 (NICD) shows that Notch signalling is active in CK lung tumours (Figure 6C). However, no Notch activity could be detected in AEC2 derived hyperplastic cells (Figures 6D and E). Gene set enrichment analysis of RNA-seq data on the SK model shows that Notch activity has decreased in neoplastic cells when compared to AEC2 (Figure 6F) (Subramanian et al., 2005). Increased expression of non-canonical Notch ligand *Dlk1*, which has been shown to inhibit Notch signalling in AEC2 cells, was observed in SK neoplastic cells (Figure S4B) (Finn et al., 2019). Notch signalling has been shown to be necessary for maintaining club cell identity (Lafkas et al., 2015). Blocking Notch activity results in reduced tumour formation in the CK model (Xu et al., 2014). These observations suggest that tumour progression is influenced by its cell of origin.

PCA shows that the neoplastic cells from the CK mice cluster with the club cells and that the neoplastic cells from the SK mice are closer to AEC2 and CC10+ AEC2 cells in their epigenetic landscapes, indicating that club and AEC2 derived tumours are in distinct epigenetic states (Figure 6G). To characterise this further, we performed BaGFoot analysis to detect differential TF activity in CC10-AEC2 and club cells isolated from normal (CC) mouse lungs (Figure 6H). And we ran a similar analysis comparing SK 4w neoplastic cells and CK (16w and 22w) neoplastic cells (Figures 6I and J). We found that the factors, like FOX family TFs, which show increased activity in club cells also show similar activity in the CK neoplastic cells. HNF, NKX and GATA family TFs show higher activity in both AEC2 and AEC2 derived neoplastic cells. We also observed peaks that are specific to either AEC2 and its tumours or club cell and its tumours (Figures 6K–P). Interestingly, we observed that club and CK neoplastic cells, but not AEC2 and SK neoplastic cells, have increased accessibility at enhancers of airway epithelial cell markers such as *Trp73* (ciliated cells), *Sox2* (pan-airway cells), *Foxi1* (ionocytes) and *Scgb1a1* (club cells) (Figures 6K, L and O) (Marshall et al., 2016; Montoro et al., 2018). This suggests that, although both AEC2 and club cells appear to form similar tumours expressing SPC, the tumours retain the epigenetic memory of their cell of origin.

Identification of a mutant-*Kras* epigenetic signature conserved across tissues

A recent study has shown that AP-1 transcription factor, *Fosl1*, is upregulated in K*ras*$^{G12D/+}$; *Tp53*$^{-/-}$ murine epidermal squamous cell carcinomas (Latil et al., 2017). It has also shown that newly accessible regions in tumours are enriched for AP-1 motifs (Latil et al., 2017). This suggests that the mechanism by which mutant-*Kras* transforms cells is conserved across tissues. We reanalysed the ATAC-seq data on hair-follicle (HF) stem cell and intrafollicular epidermis (IFE) derived tumours from (Latil et al., 2017) and confirmed that in both the cases there is a significant increase in flanking accessibility at AP-1 motif occurrences (Figures S7A and S7B). Similar to our observations in the lung, there is a significant

decrease in the nucleosome occupancy at AP-1, but not at CTCF, motif occurrences in the newly open peaks of skin tumours suggesting that AP-1 complex recruits nucleosome remodelling factors to render closed regions accessible (Figures 7A and S7C). We observed that the reduction in nucleosome occupancy at AP-1, but not CTCF, motif centre in the newly open regions correlates with the fold change of newly open regions (Figures S7D and S7E). Given the significant parallels in tumour initiation in all the four different cell types – AEC2, club, HF stem cell and IFE – we identified a conserved set of newly open regions harbouring AP-1 motifs (Figure 7B). GREAT analysis shows that these regions are involved in, among many functions, cell cycle regulation – the key hallmark of cancer attributed to mutant-*Kras* (Figure 7C) (Hanahan and Weinberg, 2000; Pylayeva-Gupta et al., 2011).

KRAS mutations, although detected in about 50% of human colon tumours, are not known to initiate them. Field cancerisation has been observed in human colonic epithelium where KRAS mutations are found in histologically normal tissue (Aivado et al., 2000; Zhu et al., 1997). Expression of mutant-*Kras* in murine intestinal epithelial cells has largely yielded similar results (Feng et al., 2011; Sansom et al., 2006; Snippert et al., 2014; Trobridge et al., 2009). To understand this difference in response to a *Kras* mutation when compared to epidermal and pulmonary epithelial cells, we characterised the changes to chromatin accessibility in the *Lgr5*+ intestinal stem cells (ISC) – purported cells of origin of carcinoma – of the intestine (Barker et al., 2009).

Intestinal tissue was harvested from *Lgr5*-CreER-EGFP; $Kras^{LSL\text{-}G12D/+}$; *Rosa26*-tdTomato mice (henceforth referred to as LK model) 5, 17 and 25 weeks after tamoxifen doses (Figure 7D) (Snippert et al., 2014). Normal histology was observed at the early time-point of 5 weeks (Figure 7E). Ribbons of lineage-labelled cells can be seen (Figure S7F). Intestinal tissue collected at later stages of 17 and 25 weeks were devoid of any neoplastic or pre-neoplastic lesions, however, increased proliferation and gland herniation could be observed (Figure S7G). We sorted *Kras*-mutant and *Kras*-WT ISCs based on GFP expression and tdTomato label from the same mouse and performed ATAC-seq (Figures S7H–J). Bivariate genomic footprinting shows an increase in flanking accessibility at AP-1 motif occurrences in the *Kras* mutant ISCs collected after 5 weeks, and a greater increase after 17–25 weeks (Figures 7F and 7G). This indicates that a mechanism – downstream of mutant-*Kras* – similar to that in AEC2 is active in the ISCs. However, the increase in flanking accessibility at AP-1 motif occurrences in the *Kras* mutant ISCs is lower than what was observed in tumour generating *Kras* mutant epidermal or pulmonary epithelial cells (Figures 1G, S3C, 4F, S7A–B and 7F–G).

DISCUSSION

In this study, we have used ATAC-seq to characterise the changes to accessible chromatin in pulmonary epithelial cells in response to an oncogenic *Kras* mutation. By analysing the initial stages of tumorigenesis in the absence of additional supportive mutations, we find that *Kras* mutation leads to a remodelled chromatin landscape of club and AEC2 cells. We find that AP-1 complex containing FOSL1 directly binds to the mSWI/SNF complex and directs it to specific regions on the genome to increase accessibility. *Kras*-mutant AEC2 cells fail to form spheroids *in vitro* when AP-1 activity is blocked using a small molecule SR

11302. *Kras* mutant AEC2 show a significant reduction in proliferation *in vivo* when treated with the same drug suggesting that AP-1 dependent chromatin remodelling is necessary for mutant-*Kras* driven tumour initiation.

We observe that a small but significant increase, about one and a half times, in the *Fosl1* transcript levels leads to a drastic increase in the protein level. This suggests that post-translational modifications to FOSL1, downstream of KRAS signalling, are at play here and need to be further characterised. We have found that all the JUN family proteins, c-JUN, JUNB and JUND bind to FOSL1 in KRAS mutant cells. It would be interesting to characterise the differences in the functions of each of the three AP-1 heterodimers. Similarly, the composition of the SWI/SNF complexes which are made up of multiple sub-units and their differential interaction with AP-1, which may be cell type specific, would be important to characterise.

Mutant-*Kras* driven transformation of club cells involves two major processes: their transdifferentiation into surfactant-producing AEC2-like state through NKX2.1 and a core-oncogenic program fuelled by AP-1 activity, as seen in AEC2 cells. A similar approach may be used to dissect the molecular processes involved in *Kras*-driven pancreatic ductal adenocarcinoma where acinar cells transdifferentiate into ductal-like cells before forming pancreatic intraepithelial neoplasia (Ardito et al., 2012; Shi et al., 2013). It is likely that a similar duo of cell-type specific transcription factor and an AP-1 dependent oncogenic program would be active here (Vallejo et al., 2017).

We observe that tumours retain an epigenetic memory of their cells of origin. *Kras*-mutant club cells, even though acquire an AEC2-like state, retain increased accessibility to putative enhancers of airway-lineage specific markers. AP-1 mediated increase in chromatin accessibility also depends on cell-type specific transcription factors, such as HES1 in club-driven tumours (Vierbuchen et al., 2017). Understanding the chromatin state of the cell of origin can also help identify novel therapeutic targets (Latil et al., 2017).

Limitations of the Study

We have mainly used two models in this study, SK and CK, where *Scgb1a1* and *Sftpc* promoters are used to activate mutant-*Kras* expression in AT2 or club cells respectively. However, in both the models, mutant-*Kras* expression is also activated in BASCs, which are present in a small number. Future studies, using lineage-tracing based methods, are necessary to establish whether the BASCs have the potential to make tumours and if AP-1 dependent mechanisms are active in them.

STAR METHODS

Resource Availability

Lead Contact—Further information and requests for reagents may be directed to and will be fulfilled by the Lead Contact, Xiling Shen (xiling.shen@duke.edu).

Materials Availability—This study did not generate new unique reagents.

Data and Code Availability

- Sequencing data generated during this study have been deposited to GEO and are publicly available as of the date of publication. Accession numbers are listed in the key resources table. Proteomics data generated during this study have been deposited to ProteomeXchange and are publicly available as of the date of publication. Accession number and DOI are listed in the key resources table. Original western blot images have been deposited at Mendeley and are publicly available as of the date of publication. The DOI is listed in the key resources table.
- This paper does not report original code.
- Any additional information required to reanalyze the data reported in this paper is available from the lead contact upon request.

Experimental Model and Subject Details

Humans—Patient lung samples were collected under Duke University Health System Institutional Review Board (IRB) approved protocols Pro00002435 and Pro00100393. All participants provided written informed consent to participate in the study.

Mice—PDX models of lung cancer were generated in accordance with the animal guidelines and with the approval of the Institutional Animal Care and Use committee (IACUC) at the Duke University Medical Center (Protocol Number A112–18-05).

All other experiments involving mice were approved by the IACUC at Duke University and conducted under protocols A286–15-11 and A235–18-10. *Sftpc*-CreER, *Scgb1a1*-CreER, *R26R*-tdTomato, *Kras*$^{LSL\text{-}G12D/+}$ and *R26R*-fGFP mice were provided by Mark Onaitis of Duke University. Aline Bozec from University of Erlangen for provided the *Fosl1*$^{fl/fl}$ mice. *Lgr5*-EGFP-IRES-creERT2 mice were purchased from Jackson Laboratory (#8875). Mice were housed, no more than 5 to a cage, on alpha-dry bedding under the supervision of the Duke Division of Laboratory Animal Resources (DLAR). The housing environment was monitored daily for temperature, humidity and light cycle. Mice were fed *ad libitum*. The mouse facility was overseen by a staff of veterinarians and vet technicians, who examined all cages on a weekly basis to ensure proper care and handling of the animals. Facility was maintained under specific pathogen free (SPF) conditions. All animals were housed in micro-isolator cages. Each rack had a cage of sentry mice that is exposed to bedding from the other cages in the room. Sentry mice were examined serologically by DLAR staff on a monthly basis. Mice were handled in accordance with the guidelines of the NIH for humane use of animals and the Duke University IACUC Committee. Only 6–10 weeks old male mice were used in lung cancer experiments as female mice do not survive until the late time points analysed in this study (Histo-pathological analysis of lung sections and isolation of primary cells for ATAC-seq, RNA-seq and qPCR). Both female and males of 6–10 weeks of age were used for the intestinal study (histo-pathological analysis of the tissue and isolation *Lgr5*-GFP+ cells for ATAC-seq)

Method details

CreER activation—Tamoxifen was dissolved in corn oil at a concentration of 20 mg/ml and stored at 4°C for a maximum time of one month. 75 mg/kg body weight doses of tamoxifen were administered to mice intraperitoneally (IP) to activate CreER. All mice used in the lung cancer study received four doses, with a gap of 48 hours between each dose, except CK 22w ones which received only two doses. *Lgr5*-CreER mice received a dose of tamoxifen per day for four consecutive days.

In SK mice, Cre activity is seen in a few AEC2 cells in the absence of any tamoxifen. Owing to the increased surfactant production, female SK mice often succumb before reaching maturity (6 weeks of age). Hence, the study has been restricted to male mice. Surfactant burden on the male mice is high 5–6 weeks after they receive tamoxifen doses. So, the study was limited up to 4 weeks post the doses.

AP-1 inhibition *in vivo*—SK mice were intraperitoneally injected with 2 mg/kg of AP-1 inhibitor SR 11302 followed by a dose of tamoxifen after two hours. The injections were repeated after 2 days after which tamoxifen doses were stopped. Mice continued to receive SR 11302 doses once every 48 hours for 3 weeks. Mice were then euthanised and lungs were harvested.

Patient Derived Xenograft—To generate lung cancer PDXs, tissue samples were washed in phosphate buffered saline (PBS), dissected into small pieces (<2 mm), and injected into the flanks of 8–10-week-old JAX NOD.CB17-PrkdcSCID-J mice obtained from the Duke University Rodent Genetic and Breeding Core (Kim et al., 2012; Uronis et al., 2012).

Lung harvest—Mice were anaesthetised using Avertin. Skin and muscular layers were cut to expose the abdominal and thoracic cavities. Descending aorta was cut to exsanguinate and euthanise the animal. Cold PBS was perfused through the cardiac right ventricle to flush the blood out of the lungs. Lungs were then removed and inflated with 4% PFA and fixed overnight at 4°C in PFA for histology. For isolation of live primary cells, lungs were instead inflated with lung/tumour dissociation buffer (Miltenyi Biotec), cut into small pieces and incubated at 37°C for 30 minutes (normal lung) or 45 minutes (lung with neoplastic growth). A single cell suspension was obtained by mechanically dissociating using gentleMACS (Miltenyi Biotec) dissociator and passing the samples through a 70 μm filter. RBCs were lysed by resuspending the cells in ACK lysis buffer and leucocytes were depleted by using anti-CD45 microbeads (Miltenyi Biotec).

To isolate AEC2 cells from CC mice, Lysotracker dye was used (der Velden et al., 2013). Briefly, dissociated lung cells were resuspended in DMEM/F12 containing Lysotracker (1 μL dye in 14 mL medium) and incubated at 37°C for 30 minutes.

Human normal lung and cancer samples were stored on ice in DMEM/F12 medium supplemented with 2% FBS until dissociation. Samples were dissociated using human tumour dissociation kit (Miltenyi Biotec) following the manufacturer's recommendation. A single cell suspension was obtained by passing the dissociated samples through a 70 μm filter. RBCs were lysed by resuspending the cells in ACK lysis buffer and leucocytes

were depleted by using anti-CD45 microbeads (Miltenyi Biotec). Samples were resuspended in PBS supplemented with 10% FBS and incubated with anti-EpCAM antibodies for 10 minutes at room temperature. Samples were then washed once in PBS supplemented with 10% FBS.

Primary cells were isolated by FACS using SONY SH800 sorter. Sytox dyes (Blue, Green, Red and AADvanced) were used to exclude dead cells.

Intestine harvest—Intestinal *Lgr5*$^{+}$ stem cells were isolated as described in (Murthy et al., 2018). Briefly, lineage labelled *Lgr5*-CreER-GFP mice were euthanised and small intestines (from duodenum to ileum) were collected. Intestinal tubes were longitudinally sectioned to expose the luminal surface and washed in cold PBS. Tissues were minced into 2–4 mm long pieces and incubated in 2 mM EDTA in PBS for 45 minutes at 4°C for 45 minutes. Samples were transferred to fresh cold PBS and vigorously shook to release crypts into the solution. Isolated crypts were further dissociated into single cells by a 30 minutes trypsin treatment at 37°C. Cell suspension was filtered using a 70 μm filter. GFP^{+} cells were isolated by FACS for further analysis.

NGS library preparation

ATAC-seq: Harvested primary cells were immediately used to prepare ATAC-seq libraries (Buenrostro et al., 2013). Briefly, isolated cells were washed in PBS and resuspended in buffer containing transposase Tn5 and incubated at 37°C for 30 minutes. Number of cells used to prepare each library has been summarised in Table S1. Tagmented DNA was PCR amplified for 10–16 cycles.

Mitochondrial DNA present in the libraries was cleaved using a CRISPR-Cas9 based method described in (Wu et al., 2016). sgRNA library targeting mitochondrial DNA was purchased from Addgene (#82480). *In vitro* transcription was performed to produce the gRNAs using MEGAshortscript Kit (Thermo Fisher Scientific). ATAC-seq libraries were treated with 10 μg Cas9 protein and 15 μg of sgRNA in a 40 μL reaction for 2 hours at 37°C. The libraries were purified using Qiaquick PCR purification kit (Qiagen) and sequenced using Illumina Hi-Seq 2500 (50 bp paired end) or Next-Seq (75 bp paired end).

RNA-seq: Total RNA was isolated from primary cells using RNeasy Mini kit (Qiagen). Samples with RIN > 9 were used for library preparation by Duke University's genomics core using KAPA stranded mRNA library prep kit. Libraries were sequenced using Illumia Hi-Seq 4000 (50 bp single end).

scRNA-seq: Lungs were collected from two CK 6w and 6 CC (control) mice injected with 4 doses of tamoxifen. Tissues were dissociated and a single cell suspensions were subjected to immune cell depletion using CD45 microbeads as described previously. fGFP^{+} cells were enriched by performing FACS in "yield-sort" mode. This mode is suitable to enrich populations found in small numbers, however, also results in contamination from other fGFP^{-} cell types. The number of fGFP^{+} cells in each lung is small and a minimum of 100,000 cells are necessary for scRNA-seq, hence the 'yield-sort' mode was chosen. fGFP^{+} cell enriched suspensions from all controls were pooled but the two tumour samples

were handled separately. Cells were then resuspended in 0.01% BSA in PBS. scRNA-seq was performed using Drop-seq protocol (Macosko et al., 2015) with modifications described in (Kobayashi et al., 2020). Briefly, single cells were encapsulated in droplets containing mRNA-capture beads by using a microfluidic chamber. Droplets were then broken by adding perfluorooctanol (Sigma) and vigorous shaking. mRNAs captured on the beads were reverse transcribed using Maxia H Minus RTase (Thermo Fisher) followed by Exonuclease I (New England Biolabs) treatment and second strand synthesis using Klenow fragment (New England Biolabs). Pre-amplification QC was performed using Terra polymerase (one cycle of 98°C for 3 minutes; 4 cycles of 98°C for 15s, 55°C for 45s and 68°C for 4 minutes; 15–17 cycles of 98°C for 15s, 57°C for 30s and 68°C for 4 minutes; one cycle of 72°C for 10 minutes and 4°C hold). Library construction PCR was performed using Nextera XT DNA library preparation kit (Illumina). PCR products were purified by double-sided 0.6x SPRI bead purification. Libraries were sequenced on Hi-Seq in 150 bp PE configuration.

Cell culture—A549 cell line was cultured in F12-K medium (Thermo Fisher) and MRC5 cells in MEM (Thermo Fisher). Culture media were supplemented with 10% FBS (Thermo Fisher) and 1% Antibiotic-Antimycotic (Thermo Fisher). Mouse KP cell lines were cultured in DMEM (Thermo Fisher) with 10% FBS and 1% Antibiotic-Antimycotic.

AEC2 cells were cultured as spheroids as described in (Barkauskas et al., 2013) with minor modifications. Isolated AEC2 cells were mixed with MRC5 cells (passage #18–25) at a 1:5 ratio and resuspended in Matrigel. 100 μL of the suspension, containing 5000 AEC2, was pipetted to a Transwell (Corning). MTEC plus medium was added to the outer side of the Transwell. Y-27632 at 1 μM was added to the medium for the first 1–2 days. 4-OHT (1.3 μg/mL concentration) was added for the first 24 hours of culture to activate CreER. After 8 days of culture, spheroids were imaged using a Leica fluorescent microscope with 4x objective lens.

AP-1 inhibitors SR11302 and T-5224 were added to organoids at 10 μM and 100 μM concentration, respectively.

Club-like cells isolated from CK mice were cultured in Matrigel similar to AEC2 cells.

Nuclear protein extraction—Nuclear protein was extracted from A549 cells (WT or FOSL1-FLAG) as described in (Erdoğan et al., 2016). 4 × 10 cm dishes of A549 (with or without FOSL1-FLAG modification) cells were trypsinised and resuspended in hypotonic lysis buffer (10 mM HEPES pH 7.9, 1.5 mM MgCl2, and 10 mM KCl, 10 mM DTT and 1x protease inhibitor cocktail). After 15 minutes of incubation on ice, Igepal was added to a final concentration of 0.6%. Samples were vortexed and spun down at 10,000 g for 30s. Nuclear buffer (50 mM Tris-HCl, pH 7.5; 150 mM NaCl, 0.5% Triton-X 100 and 1x protease inhibitor cocktail) was added to the pellet and sonicated for 5s twice using a probe-based sonicator.

Immunoprecipitation (IP)—IP was performed to purify FLAG tagged FOSL1 protein immediately after extracting the nuclear protein from A549 cells. Magnetic anti-Flag M2 beads (Sigma) were washed thrice using TBS and incubated with nuclear extract for 60

minutes at room temperature. Beads were then washed three times in TBS. Bead bound proteins were eluted by competition with 3X-Flag peptides.

Mass spectrometry of isolated proteins was performed by the proteomics core facility at Duke University GCB and the data were analysed using Scaffold 4 software.

Western Blotting—The assay was performed as described in (Xi et al., 2019). In brief, immunoprecipitated samples were electrophoresed on Mini Protean Stain free gels (Bio-rad). Proteins were then transferred to low fluorescence PVDF membrane (Bio-rad). Membrane was blocked using 5% non-fat milk in TBS for an hour at room temperature. Incubation with primary antibodies was performed overnight at 4°C followed by three washes in TBST (TBS + 0.1% Tween-20). HRP conjugated secondary antibodies were added for an hour at room temperature and the membrane was washed thrice in TBST. Chemiluminescent signal was produced at antibody bound sites using SuperSignal West femto (Thermo Fisher) and detected using Chemi-Doc (Bio-rad). Images were analysed using Image Lab (Bio-rad) and Fiji (ImageJ) software.

Mint-ChIP—tdTomato^{+} cells from SK 4w mouse lung were isolated by FACS as described above. Cultured KP cells were dissociated using Trypsin (Thermo Fisher). Approximately 500,000 cells were used from each sample. FOSL1 binding sites were identified using the Mint-ChIP assay (Kobayashi et al., 2020; van Galen et al., 2016). Updated version of the Mint-ChIP protocol (version 3) was used (https://dx.doi.org/10.17504/protocols.io.wbefaje). Cells were lysed on ice for one hour followed by digestion with 300 units of MNase for 10 minutes at 37°C. T7 adapters were then ligated, and samples were incubated with anti-FOSL1 antibody overnight at 4°C. Chromatin fragments bound to antibody were isolated using protein A/G Dynabeads and digested with proteinase K for one hour at 63°C. DNA was purified using 1x SPRI bead clean-up. In vitro transcription was performed using T7 RNA polymerase (New England BioLabs). RNA was purified using silane beads followed by reverse transcription using Superscript III enzyme (Thermo Fisher). cDNA was purified using SPRI beads and used for library preparation PCR using Terra DNA polymerase (Takara). Size selection of libraries was performed using SPRI beads. Libraries were sequenced using NovaSeq S4 flow cell in 150 bp PE configuration.

Histology—Fixed samples were dehydrated using a series of increasing concentrations of ethanol. Ethanol was then removed by incubation with Xylene and then embedded in paraffin. 4–8 μm sections were cut from embedded blocks and placed on slides. Slides were baked at 60°C for an hour and deparaffinised using xylene and dried using ethanol and rehydrated. H&E staining was performed using standard methods.

Immunostaining was performed as described in (Murthy et al., 2018). Briefly, antigen retrieval was performed using Tris-EDTA buffer at pH 9 (Vector Labs). Serum free protein block (Dako) was applied for 10 minutes at room temperature. Slides were then incubated in endogenous peroxide block (Dako). Sections were then incubated with primary antibodies overnight at 4°C. Slides were washed three times in PBS and incubated with secondary antibodies for an hour at room temperature. TSA amplification (Perkin Elmer) was performed when probing for NICD and FOSL1. Autofluorescence was quenched

using TrueBlack reagent (Biotium). Mounting medium containing DAPI (Vector Labs) was used and slides were imaged using Zeiss 780i confocal microscope or Zeiss Axio Imager epifluorescence microscope.

qRT-PCR—Total RNA was extracted from isolated cells using RNeasy Mini Kit (Qiagen). Primers to detect *Scgb1a1*, *Fosl1*, *Sftpc* and *Actin* were purchased from Genecopoeia.

Quantification and Statistical Analysis

General—Unless otherwise specified, data are presented as Mean ± Standard Deviation. Student's t-test was performed to compare two groups and Dunnett's test was used to compare multiple groups to a single control, and a *P*-value threshold of 0.05 was used to determine statistical significance.

ATAC-seq—ATAC-seq data were processed using the pipeline developed in (Koh et al., 2016) with default parameters. 75 bp PE reads were trimmed to 50 bp PE using FASTX toolkit (http://hannonlab.cshl.edu/fastx_toolkit/) before analysing them. Reads were aligned to mm10 (mouse) or GRCh38 (human) genome using Bowtie 2 (Langmead and Salzberg, 2012). Duplicate and mitochondrial reads were removed. And peaks were called using MACS2 software. Peaks were annotated using HOMER (Heinz et al., 2010). Sample quality statistics are provided in Supplementary Table 1.

Publicly available ATAC-seq data on A549 cells is single-ended (Consortium, 2012). To ensure compatibility, only one end (Read 1) of human normal and tumour ATAC-seq data generated for this article was processed.

Differential peak calling and annotation—Differential peaks were identified using Diffbind with a minimum of 2 biological replicates for each case. (Ross-Innes et al., 2012). Unless otherwise stated, peaks with FDR corrected *P*-value < 0.05 and $\log_2$ |Fold Change| > 1 were considered differentially accessible. Others were considered constitutively open peaks (Denny et al., 2016). Principal component analysis was performed using dba.PlotPCA command in the DiffBind package. Differential peaks were annotated using annotatePeaks.pl and enriched transcription factor motifs were identified using findMotifsGenome.pl programs of HOMER package (Heinz et al., 2010). Peaks were assigned to their putative effector genes using GREAT (McLean et al., 2010) online tool using the whole genome as background.

Bivariate Genomic Footprinting (BaGFoot)—BaGFoot analysis was performed following the algorithm published in (Baek et al., 2017). mm10 genome was used as reference. Aligned and filtered ATAC-seq reads from biological replicates were pooled to create a single *.bam file for each condition and used for pairwise BaGFoot analysis.

As the publicly available ATAC-seq data on A549 cells is single-ended, BaGFoot analysis was not performed on human samples.

Nucleosome occupancy—Broadpeak files of all biological replicates per condition were merged and extended by 100bp on each side. Filtered Bam files were similarly pooled

and used as inputs to the NucleoATAC program (Schep et al., 2015) to obtain nucleosome occupancy scores. Average nucleosome occupancy was calculated around AP-1 or CTCF motif centres in newly open peaks ($\log_2$ |Fold Change| ≥ 1 and q-value < 0.05) and constitutive peaks.

Identification of collaborating transcription factors—Cell type specific transcription factors collaborating with AP-1 were identified as described in (Vierbuchen et al., 2017). 220 bp regions centred around AP-1 motif occurrences (pooled occurrences of FOS, FOSB, FOSL1, FOSL2, JUN, JUNB and JUND motifs) were used as input to the Centrimo package to identify the TF motif enrichment in the neighbourhood of putative AP-1 binding sites (Bailey et al., 2009). Regions with increased accessibility only in CK neoplastic cells, SK neoplastic cells or both are denoted by subscripts C, S and I respectively. Log adjusted P-value, denoted by P, was obtained for motifs enriched in the three peak-sets. Relative enrichment score (R) of a motif was calculated for each of the three peak-sets using the equation, $R_C = -P_C P_{C,S}^{norm} P_{C,I}^{norm}$, where $P_{C,S}^{norm} = \left(\frac{P_C}{P_S \max\left(\frac{P_C}{P_S}\right)}\right)$. TF motifs were rank-ordered using the relative enrichment scores and the top 20 were selected from each peak-set. Representative motifs from this set were used to make a bubble plot.

RNA-Seq—RNA-seq data were analysed using the RNA Express package available on Basespace (Illumina). Briefly, reads were aligned to the mm10 genome using STAR and differentially expressed genes were identified using DESeq2 (Dobin et al., 2013; Love et al., 2014). Transcripts with |FC| > 1.5 and q value < 0.05 were considered to be differentially expressed.

scRNA-Seq—Drop-seq data generated in this study were analysed using dropSeqPipe as described in (Kobayashi et al., 2020). Briefly, reads were aligned to mm10 genome and UMI counts were obtained. Counts were imported into Seurat for further analysis. Data were normalised using SCTransform (Hafemeister and Satija, 2019) before performing PCA and UMAP dimensional reductions, and identifying clusters. Non-epithelial cells were excluded from the analysis based on the expression of *Pecam1*, *Ptprc*, *Pdgfra*, *Pdgfrb* and *Acta2*. Cell barcodes of interest were used as input to velocyto.py program (La Manno et al., 2018) for RNA velocity analysis. Genes enriched in club-like tumour cells when compared to normal club cells were identified using Seurat's FindMarkers() function and enriched pathways were identified using WebGestalt package (Liao et al., 2019). PID gene-sets enriched in all tumour cell-types was performed using Variance adjusted Mahalanobis method (Frost, 2020).

Mint-ChIP—FASTQ files were processed and aligned to the mm10 genome as described in (Kobayashi et al., 2020) using this pipeline: https://github.com/jianhong/MintChIP. Two technical replicates were performed for each of the two KP cell-lines. Data from the replicates were merged. Signal tracks were calculated using deepTools bamCoverage() command and visualised on Integrative Genomics Viewer (Ramírez et al., 2014; Robinson et al., 2011). Consensus FOSL1 binding sites were calculated based on the presence of the

binding site in at least two of the three samples (one SK 4w and 2 KP samples) in R using rtracklayer and GenomicRanges programs.

Histopathology—H&E stained images of lung lobes were scanned using a 20x or 40x objective on Aperio Scanscope slide scanner. Various histopathological features were annotated using Aperio Imagescope software based on the guidelines in (Nikitin et al., 2004). Hypertrophic bronchiolar regions were clubbed with the normal bronchioles. No distinction was made between adenoma and adenocarcinoma during quantification. Area occupied by each feature was measured and normalised to the total lobe area. A minimum of two lobes per mouse and 3 mice per time point were analysed.

Tumour initiation assay—Images of spheroids were analysed using Fiji. Only tdTomato^{+} spheroids greater than 35 μm in diameter were quantified. A minimum of 3 technical replicates were analysed for each experiment.

Supplementary Material

Refer to Web version on PubMed Central for supplementary material.

ACKNOWLEDGEMENTS

We thank Chris Counter, David MacAlpine, Dinesh Manandhar, Anders Dohlman, Alex Barrera, Charles Gersbach, Lingchong You, Yan Han, Xia Xu, Wayne Glover, Kun Xiang, Ergang Wang and Patrice McDermott of Duke University for their invaluable assistance. We thank Mark Onaitis of Duke University for providing *Sftpc*-CreER, LSL-*Kras*^{G12D}, *Scgb1a1*-CreER, *R26R*-tdTomato and *R26R*-fGFP mouse lines. We thank the Genomic analysis and Proteomics core facilities at Duke University GCB for their help with Next-Generation Sequencing and Mass Spectrometry respectively. We thank Tyler Jacks for providing mouse KP cell line. This work was funded by NIH U01 CA217514, U01 CA214300, and R35 GM122465 to XS and DFG-SPP microbone (BO3811–1/7) grant to AB.

REFERENCES

Adamson JS, Senior RM, and Merrill T (1969). Alveolar cell carcinoma: An electron microscopic study. American Review of Respiratory Disease 100, 550–557.

Aivado M, Gynes M, Gorelov V, Schmidt W, Röher H, and Goretzki P (2000). " Field cancerization"--an additional phenomenon in development of colon tumors? K-ras codon 12 mutations in normal colonic mucosa of patients with colorectal neoplasms. Der Chirurg; Zeitschrift fur alle Gebiete der operativen Medizen 71, 1230–1234; discussion 1234–1235. [PubMed: 11077584]

Allen J, Hao S, Sears CL, and Timp W (2019). Epigenetic changes induced by Bacteroides fragilis toxin. Infection and immunity 87, e00447–00418. [PubMed: 30885929]

Ardito CM, Grüner BM, Takeuchi KK, Lubeseder-Martellato C, Teichmann N, Mazur PK, DelGiorno KE, Carpenter ES, Halbrook CJ, and Hall JC (2012). EGF receptor is required for KRAS-induced pancreatic tumorigenesis. Cancer cell 22, 304–317. [PubMed: 22975374]

Avila PC (2011). Plasticity of airway epithelial cells. Journal of Allergy and Clinical Immunology 128, 1225–1226.

Baek S, Goldstein I, and Hager GL (2017). Bivariate Genomic Footprinting Detects Changes in Transcription Factor Activity. Cell Reports 19, 1710–1722. [PubMed: 28538187]

Bailey TL, Boden M, Buske FA, Frith M, Grant CE, Clementi L, Ren J, Li WW, and Noble WS (2009). MEME SUITE: tools for motif discovery and searching. Nucleic acids research 37, W202–W208. [PubMed: 19458158]

Barkauskas CE, Cronce MJ, Rackley CR, Bowie EJ, Keene DR, Stripp BR, Randell SH, Noble PW, and Hogan B (2013). Type 2 alveolar cells are stem cells in adult lung. Journal of Clinical Investigation 123, 3025–3036.

Barker N, Ridgway RA, van Es JH, van de Wetering M, Begthel H, van den Born M, Danenberg E, Clarke AR, Sansom OJ, and Clevers H (2009). Crypt stem cells as the cells-of-origin of intestinal cancer. Nature 457, 608. [PubMed: 19092804]

Bell O, Tiwari VK, Thomä NH, and Schübeler D (2011). Determinants and dynamics of genome accessibility. Nature Reviews Genetics 12, 554.

Buenrostro JD, Corces MR, Lareau CA, Wu B, Schep AN, Aryee MJ, Majeti R, Chang HY, and Greenleaf WJ (2018). Integrated Single-Cell Analysis Maps the Continuous Regulatory Landscape of Human Hematopoietic Differentiation. Cell 173, 1535–1548.e1516. [PubMed: 29706549]

Buenrostro JD, Giresi PG, Zaba LC, Chang HY, and Greenleaf WJ (2013). Transposition of native chromatin for fast and sensitive epigenomic profiling of open chromatin, DNA-binding proteins and nucleosome position. Nature methods 10, 1213. [PubMed: 24097267]

Chen S, Lake BB, and Zhang K (2019). Linking transcriptome and chromatin accessibility in nanoliter droplets for single-cell sequencing. bioRxiv, 692608.

Coalson JJ, Mohr J, Pirtle J, Dee A, and Rhoades E (1970). Electron microscopy of neoplasms in the lung with special emphasis on the alveolar cell carcinoma. American Review of Respiratory Disease 101, 181–197.

Consortium EP (2012). An integrated encyclopedia of DNA elements in the human genome. Nature 489, 57. [PubMed: 22955616]

Corces MR, Granja JM, Shams S, Louie BH, Seoane JA, Zhou W, Silva TC, Groeneveld C, Wong CK, and Cho SW (2018). The chromatin accessibility landscape of primary human cancers. Science 362.

Cox AD, Fesik SW, Kimmelman AC, Luo J, and Der CJ (2014). Drugging the undruggable RAS: mission possible? Nature reviews Drug discovery 13, 828. [PubMed: 25323927]

Denny SK, Yang D, Chuang C-H, Brady JJ, Lim JS, Grüner BM, Chiou S-H, Schep AN, Baral J, and Hamard C (2016). Nfib promotes metastasis through a widespread increase in chromatin accessibility. Cell 166, 328–342. [PubMed: 27374332]

der Velden JL, Bertoncello I, and McQualter JL (2013). LysoTracker is a marker of differentiated alveolar type II cells. Respiratory Research 14, 1–7. [PubMed: 23289668]

Dermer GB (1981). Autoradiography of cellular glycoproteins reveals histogenesis of bronchogenic adenocarcinomas. Cancer 47, 2000–2006. [PubMed: 7226094]

Desai TJ, Brownfield DG, and Krasnow MA (2014). Alveolar progenitor and stem cells in lung development, renewal and cancer. Nature 507, 190. [PubMed: 24499815]

Devall M, Jennelle LT, Bryant J, Bien S, Peters U, Powell S, and Casey G (2020). Modeling the effect of prolonged ethanol exposure on global gene expression and chromatin accessibility in normal 3D colon organoids. PloS one 15, e0227116. [PubMed: 31951625]

Dimitrova N, Gocheva V, Bhutkar A, Resnick R, Jong RM, Miller KM, Bendor J, and Jacks T (2016). Stromal expression of miR-143/145 promotes neoangiogenesis in lung cancer development. Cancer discovery 6, 188–201. [PubMed: 26586766]

Dobin A, Davis CA, Schlesinger F, Drenkow J, Zaleski C, Jha S, Batut P, Chaisson M, and Gingeras TR (2013). STAR: ultrafast universal RNA-seq aligner. Bioinformatics 29, 15–21. [PubMed: 23104886]

Eferl R, Hoebertz A, Schilling AF, Rath M, Karreth F, Kenner L, Amling M, and Wagner EF (2004). The Fos-related antigen Fra-1 is an activator of bone matrix formation. The EMBO journal 23, 2789–2799. [PubMed: 15229648]

Eferl R, and Wagner EF (2003). AP-1: a double-edged sword in tumorigenesis. Nature Reviews Cancer 3, 859. [PubMed: 14668816]

Elangovan IM, Vaz M, Tamatam CR, Potteti HR, Reddy NM, and Reddy SP (2018). FOSL1 promotes Kras-induced lung cancer through amphiregulin and cell survival gene regulation. American journal of respiratory cell and molecular biology 58, 625–635. [PubMed: 29112457]

Erdoğan Ö, Xie L, Wang L, Wu B, Kong Q, Wan Y, and Chen X (2016). Proteomic dissection of LPS-inducible, PHF8-dependent secretome reveals novel roles of PHF8 in TLR4-induced acute inflammation and T cell proliferation. Scientific reports 6, 24833. [PubMed: 27112199]

Fanjul A, Dawson MI, Hobbs PD, Jong L, Cameron JF, Harlev E, Graupner G, Lu X-P, and Pfahl M (1994). A new class of retinoids with selective inhibition of AP-1 inhibits proliferation. Nature 372, 107. [PubMed: 7969403]

Feng Y, Bommer GT, Zhao J, Green M, Sands E, Zhai Y, Brown K, Burberry A, Cho KR, and Fearon ER (2011). Mutant KRAS promotes hyperplasia and alters differentiation in the colon epithelium but does not expand the presumptive stem cell pool. Gastroenterology 141, 1003–1013. e1010. [PubMed: 21699772]

Finn J, Sottoriva K, Pajcini KV, Kitajewski JK, Chen C, Zhang W, Malik AB, and Liu Y (2019). Dlk1-Mediated Temporal Regulation of Notch Signaling Is Required for Differentiation of Alveolar Type II to Type I Cells during Repair. Cell reports 26, 2942–2954. e2945. [PubMed: 30865885]

Frost HR (2020). Variance-adjusted Mahalanobis (VAM): a fast and accurate method for cell-specific gene set scoring. Nucleic acids research 48, e94–e94. [PubMed: 32633778]

Ge Y, Gomez NC, Adam RC, Nikolova M, Yang H, Verma A, Lu CP-J, Polak L, Yuan S, and Elemento O (2017). Stem cell lineage infidelity drives wound repair and cancer. Cell 169, 636–650. e614. [PubMed: 28434617]

Hafemeister C, and Satija R (2019). Normalization and variance stabilization of single-cell RNA-seq data using regularized negative binomial regression. Genome biology 20, 1–15. [PubMed: 30606230]

Hanahan D, and Weinberg RA (2000). The hallmarks of cancer. cell 100, 57–70. [PubMed: 10647931]

Heavey S, Godwin P, Baird A-M, Barr MP, Umezawa K, Cuffe S, Finn SP, O'Byrne KJ, and Gately K (2014). Strategic targeting of the PI3K-NFκB axis in cisplatin-resistant NSCLC. Cancer biology & therapy 15, 1367–1377. [PubMed: 25025901]

Heinz S, Benner C, Spann N, Bertolino E, Lin YC, Laslo P, Cheng JX, Murre C, Singh H, and Glass CK (2010). Simple combinations of lineage-determining transcription factors prime cis-regulatory elements required for macrophage and B cell identities. Molecular cell 38, 576–589. [PubMed: 20513432]

Huang C, Ma W-Y, Dawson MI, Rincon M, Flavell RA, and Dong Z (1997). Blocking activator protein-1 activity, but not activating retinoic acid response element, is required for the antitumor promotion effect of retinoic acid. Proceedings of the National Academy of Sciences 94, 5826–5830.

Ito T, Yamauchi M, Nishina M, Yamamichi N, Mizutani T, Ui M, Murakami M, and Iba H (2001). Identification of SWI· SNF complex subunit BAF60a as a determinant of the transactivation potential of Fos/Jun dimers. Journal of Biological Chemistry 276, 2852–2857.

Jackson EL, Olive KP, Tuveson DA, Bronson R, Crowley D, Brown M, and Jacks T (2005). The differential effects of mutant p53 alleles on advanced murine lung cancer. Cancer research 65, 10280–10288. [PubMed: 16288016]

Jackson EL, Willis N, Mercer K, Bronson RT, Crowley D, Montoya R, Jacks T, and Tuveson DA (2001). Analysis of lung tumor initiation and progression using conditional expression of oncogenic K-ras. Genes & development 15, 3243–3248. [PubMed: 11751630]

Jain R, Barkauskas CE, Takeda N, Bowie EJ, Aghajanian H, Wang Q, Padmanabhan A, Manderfield LJ, Gupta M, and Li D (2015). Plasticity of Hopx+ type I alveolar cells to regenerate type II cells in the lung. Nature communications 6, 6727.

Junttila MR, Karnezis AN, Garcia D, Madriles F, Kortlever RM, Rostker F, Swigart LB, Pham DM, Seo Y, and Evan GI (2010). Selective activation of p53-mediated tumour suppression in high-grade tumours. Nature 468, 567. [PubMed: 21107427]

Kamijo T, Zindy F, Roussel MF, Quelle DE, Downing JR, Ashmun RA, Grosveld G, and Sherr CJ (1997). Tumor suppression at the mouse INK4a locus mediated by the alternative reading frame product p19 ARF. Cell 91, 649–659. [PubMed: 9393858]

Kelso TW, Porter DK, Amaral ML, Shokhirev MN, Benner C, and Hargreaves DC (2017). Chromatin accessibility underlies synthetic lethality of SWI/SNF subunits in ARID1A-mutant cancers. Elife 6, e30506. [PubMed: 28967863]

Khan A, Fornes O, Stigliani A, Gheorghe M, Castro-Mondragon JA, van der Lee R, Bessy A, Cheneby J, Kulkarni SR, and Tan G (2017). JASPAR 2018: update of the open-access database

of transcription factor binding profiles and its web framework. Nucleic acids research 46, D260–D266.

Kim MK, Osada T, Barry WT, Yang XY, Freedman JA, Tsamis KA, Datto M, Clary BM, Clay T, and Morse MA (2012). Characterization of an oxaliplatin sensitivity predictor in a preclinical murine model of colorectal cancer. Molecular cancer therapeutics 11, 1500–1509. [PubMed: 22351745]

Kobayashi Y, Tata A, Konkimalla A, Katsura H, Lee RF, Ou J, Banovich NE, Kropski JA, and Tata PR (2020). Persistence of a regeneration-associated, transitional alveolar epithelial cell state in pulmonary fibrosis. Nature cell biology 22, 934–946. [PubMed: 32661339]

Koh PW, Sinha R, Barkal AA, Morganti RM, Chen A, Weissman IL, Ang LT, Kundaje A, and Loh KM (2016). An atlas of transcriptional, chromatin accessibility, and surface marker changes in human mesoderm development. Scientific data 3, 160109. [PubMed: 27996962]

Kumar PA, Hu Y, Yamamoto Y, Hoe NB, Wei TS, Mu D, Sun Y, Joo LS, Dagher R, and Zielonka EM (2011). Distal airway stem cells yield alveoli in vitro and during lung regeneration following H1N1 influenza infection. Cell 147, 525–538. [PubMed: 22036562]

Kwon M. c., and Berns A (2013). Mouse models for lung cancer. Molecular Oncology 7, 165–177. [PubMed: 23481268]

La Manno G, Soldatov R, Zeisel A, Braun E, Hochgerner H, Petukhov V, Lidschreiber K, Kastriti ME, Lönnerberg P, and Furlan A (2018). RNA velocity of single cells. Nature 560, 494–498. [PubMed: 30089906]

Lafkas D, Shelton A, Chiu C, de Leon Boenig G, Chen Y, Stawicki SS, Siltanen C, Reichelt M, Zhou M, and Wu X (2015). Therapeutic antibodies reveal Notch control of transdifferentiation in the adult lung. Nature 528, 127. [PubMed: 26580007]

Langmead B, and Salzberg SL (2012). Fast gapped-read alignment with Bowtie 2. Nature methods 9, 357. [PubMed: 22388286]

Latil M, Nassar D, Beck B, Boumahdi S, Wang L, Brisebarre A, Dubois C, Nkusi E, Lenglez S, and Checinska A (2017). Cell-type-specific chromatin states differentially prime squamous cell carcinoma tumor-initiating cells for epithelial to mesenchymal transition. Cell stem cell 20, 191–204. e195. [PubMed: 27889319]

Lawrence M, Gentleman R, and Carey V (2009). rtracklayer: an R package for interfacing with genome browsers. Bioinformatics 25, 1841–1842. [PubMed: 19468054]

Lawrence M, Huber W, Pages H, Aboyoun P, Carlson M, Gentleman R, Morgan MT, and Carey VJ (2013). Software for computing and annotating genomic ranges. PLoS computational biology 9, e1003118. [PubMed: 23950696]

Li H, Handsaker B, Wysoker A, Fennell T, Ruan J, Homer N, Marth G, Abecasis G, and Durbin R (2009). The sequence alignment/map format and SAMtools. Bioinformatics 25, 2078–2079. [PubMed: 19505943]

Liao Y, Smyth GK, and Shi W (2014). featureCounts: an efficient general purpose program for assigning sequence reads to genomic features. Bioinformatics (Oxford, England) 30, 923–930.

Liao Y, Wang J, Jaehnig EJ, Shi Z, and Zhang B (2019). WebGestalt 2019: gene set analysis toolkit with revamped UIs and APIs. Nucleic acids research 47, W199–W205. [PubMed: 31114916]

Love MI, Huber W, and Anders S (2014). Moderated estimation of fold change and dispersion for RNA-seq data with DESeq2. Genome biology 15, 550. [PubMed: 25516281]

Macosko EZ, Basu A, Satija R, Nemesh J, Shekhar K, Goldman M, Tirosh I, Bialas AR, Kamitaki N, and Martersteck EM (2015). Highly parallel genome-wide expression profiling of individual cells using nanoliter droplets. Cell 161, 1202–1214. [PubMed: 26000488]

Maeda Y, Tsuchiya T, Hao H, Tompkins DH, Xu Y, Mucenski ML, Du L, Keiser AR, Fukazawa T, and Naomoto Y (2012). Kras G12D and Nkx2–1 haploinsufficiency induce mucinous adenocarcinoma of the lung. The Journal of clinical investigation 122, 4388–4400. [PubMed: 23143308]

Makino H, Seki S, Yahara Y, Shiozawa S, Aikawa Y, Motomura H, Nogami M, Watanabe K, Sainoh T, Ito H, et al. (2017). A selective inhibition of c-Fos/activator protein-1 as a potential therapeutic target for intervertebral disc degeneration and associated pain. Sci Rep 7, 16983. [PubMed: 29208967]

Marshall CB, Mays DJ, Beeler JS, Rosenbluth JM, Boyd KL, Guasch GLS, Shaver TM, Tang LJ, Liu Q, and Shyr Y (2016). p73 is required for multiciliogenesis and regulates the Foxj1-associated gene network. Cell reports 14, 2289–2300. [PubMed: 26947080]

McLean CY, Bristor D, Hiller M, Clarke SL, Schaar BT, Lowe CB, Wenger AM, and Bejerano G (2010). GREAT improves functional interpretation of cis-regulatory regions. Nature biotechnology 28, 495.

Montoro DT, Haber AL, Biton M, Vinarsky V, Lin B, Birket SE, Yuan F, Chen S, Leung HM, and Villoria J (2018). A revised airway epithelial hierarchy includes CFTR-expressing ionocytes. Nature 560, 319. [PubMed: 30069044]

Morris SA (2019). The evolving concept of cell identity in the single cell era. Development 146, dev169748. [PubMed: 31249002]

Murthy PKL, Srinivasan T, Bochter MS, Xi R, Varanko AK, Tung K-L, Semerci F, Xu K, Maletic-Savatic M, and Cole SE (2018). Radical and lunatic fringes modulate notch ligands to support mammalian intestinal homeostasis. eLife 7, e35710. [PubMed: 29629872]

Muzumdar MD, Dorans KJ, Chung KM, Robbins R, Tammela T, Gocheva V, Li CM-C, and Jacks T (2016). Clonal dynamics following p53 loss of heterozygosity in Kras-driven cancers. Nature communications 7, 12685.

Nabhan AN, Brownfield DG, Harbury PB, Krasnow MA, and Desai TJ (2018). Single-cell Wnt signaling niches maintain stemness of alveolar type 2 cells. Science 359, 1118–1123. [PubMed: 29420258]

Nakatsuka T, Tateishi K, Kudo Y, Yamamoto K, Nakagawa H, Fujiwara H, Takahashi R, Miyabayashi K, Asaoka Y, and Tanaka Y (2017). Impact of histone demethylase KDM3A-dependent AP-1 transactivity on hepatotumorigenesis induced by PI3K activation. Oncogene 36, 6262–6271. [PubMed: 28692045]

Nikitin AY, Alcaraz A, Anver MR, Bronson RT, Cardiff RD, Dixon D, Fraire AE, Gabrielson EW, Gunning WT, and Haines DC (2004). Classification of proliferative pulmonary lesions of the mouse: recommendations of the mouse models of human cancers consortium. Cancer research 64, 2307–2316. [PubMed: 15059877]

Pylayeva-Gupta Y, Grabocka E, and Bar-Sagi D (2011). RAS oncogenes: weaving a tumorigenic web. Nature Reviews Cancer 11, 761. [PubMed: 21993244]

Quinlan AR, and Hall IM (2010). BEDTools: a flexible suite of utilities for comparing genomic features. Bioinformatics (Oxford, England) 26, 841–842.

Ramírez F, Dündar F, Diehl S, Grüning BA, and Manke T (2014). deepTools: a flexible platform for exploring deep-sequencing data. Nucleic acids research 42, W187–W191. [PubMed: 24799436]

Rawlins EL, and Hogan BL (2006). Epithelial stem cells of the lung: privileged few or opportunities for many? Development 133, 2455–2465. [PubMed: 16735479]

Rawlins EL, Okubo T, Xue Y, Brass DM, Auten RL, Hasegawa H, Wang F, and Hogan BL (2009). The role of Scgb1a1+ Clara cells in the long-term maintenance and repair of lung airway, but not alveolar, epithelium. Cell stem cell 4, 525–534. [PubMed: 19497281]

Robinson JT, Thorvaldsdóttir H, Winckler W, Guttman M, Lander ES, Getz G, and Mesirov JP (2011). Integrative genomics viewer. Nat Biotechnol 29, 24–26. [PubMed: 21221095]

Robinson MD, McCarthy DJ, and Smyth GK (2010). edgeR: a Bioconductor package for differential expression analysis of digital gene expression data. Bioinformatics (Oxford, England) 26, 139–140.

Rohart F, Gautier B, Singh A, and Lê Cao K-A (2017). mixOmics: An R package for 'omics feature selection and multiple data integration. PLoS computational biology 13, e1005752. [PubMed: 29099853]

Ross-Innes CS, Stark R, Teschendorff AE, Holmes KA, Ali HR, Dunning MJ, Brown GD, Gojis O, Ellis IO, and Green AR (2012). Differential oestrogen receptor binding is associated with clinical outcome in breast cancer. Nature 481, 389. [PubMed: 22217937]

Rowbotham SP, and Kim CF (2014). Diverse cells at the origin of lung adenocarcinoma. 111, 4745–4746.

Sansom OJ, Meniel V, Wilkins JA, Cole AM, Oien KA, Marsh V, Jamieson TJ, Guerra C, Ashton GH, Barbacid M, et al. (2006). Loss of Apc allows phenotypic manifestation of the transforming

properties of an endogenous K-ras oncogene in vivo. Proceedings of the National Academy of Sciences 103, 14122–14127.

Sarkisian CJ, Keister BA, Stairs DB, Boxer RB, Moody SE, and Chodosh LA (2007). Dose-dependent oncogene-induced senescence in vivo and its evasion during mammary tumorigenesis. Nature Cell Biology 9, 493. [PubMed: 17450133]

Schep AN, Buenrostro JD, Denny SK, Schwartz K, Sherlock G, and Greenleaf WJ (2015). Structured nucleosome fingerprints enable high-resolution mapping of chromatin architecture within regulatory regions. Genome Res 25, 1757–1770. [PubMed: 26314830]

Schindelin J, Arganda-Carreras I, Frise E, Kaynig V, Longair M, Pietzsch T, Preibisch S, Rueden C, Saalfeld S, and Schmid B (2012). Fiji: an open-source platform for biological-image analysis. Nature methods 9, 676. [PubMed: 22743772]

Seo J, Koçak DD, Bartelt LC, Williams CA, Barrera A, Gersbach CA, and Reddy TE (2021). AP-1 subunits converge promiscuously at enhancers to potentiate transcription. Genome research 31, 538–550. [PubMed: 33674350]

Serrano M, Lin AW, McCurrach ME, Beach D, and Lowe SW (1997). Oncogenic ras provokes premature cell senescence associated with accumulation of p53 and p16INK4a. Cell 88, 593–602. [PubMed: 9054499]

Shapiro E, Biezuner T, and Linnarsson S (2013). Single-cell sequencing-based technologies will revolutionize whole-organism science. Nature Reviews Genetics 14, 618.

Shaulian E, and Karin M (2001). AP-1 in cell proliferation and survival. Oncogene 20, 2390. [PubMed: 11402335]

Sherwood RI, Hashimoto T, O'donnell CW, Lewis S, Barkal AA, Van Hoff JP, Karun V, Jaakkola T, and Gifford DK (2014a). Discovery of directional and nondirectional pioneer transcription factors by modeling DNase profile magnitude and shape. Nature biotechnology 32, 171.

Sherwood RI, Hashimoto T, O'Donnell CW, Lewis S, Barkal AA, van Hoff JP, Karun V, Jaakkola T, and Gifford DK (2014b). Discovery of directional and nondirectional pioneer transcription factors by modeling DNase profile magnitude and shape. Nature biotechnology 32, 171–178.

Shi G, DiRenzo D, Qu C, Barney D, Miley D, and Konieczny SF (2013). Maintenance of acinar cell organization is critical to preventing Kras-induced acinar-ductal metaplasia. Oncogene 32, 1950–1958. [PubMed: 22665051]

Snippert HJ, Schepers AG, van Es JH, Simons BD, and Clevers H (2014). Biased competition between Lgr5 intestinal stem cells driven by oncogenic mutation induces clonal expansion. EMBO reports 15, 62–69. [PubMed: 24355609]

Spella M, Lilis I, Pepe MA, Chen Y, Armaka M, Lamort A-S, Zazara DE, Roumelioti F, Vreka M, and Kanellakis NI (2019). Club cells form lung adenocarcinomas and maintain the alveoli of adult mice. eLife 8, e45571. [PubMed: 31140976]

Stark R, and Brown G (2011). DiffBind: differential binding analysis of ChIP-Seq peak data. R package version 100, 4–3.

Stuart T, Butler A, Hoffman P, Hafemeister C, Papalexi E, Mauck III WM, Hao Y, Stoeckius M, Smibert P, and Satija R (2019). Comprehensive Integration of Single-Cell Data. Cell.

Subramanian A, Tamayo P, Mootha VK, Mukherjee S, Ebert BL, Gillette MA, Paulovich A, Pomeroy SL, Golub TR, Lander ES, et al. (2005). Gene set enrichment analysis: A knowledge-based approach for interpreting genome-wide expression profiles. Proceedings of the National Academy of Sciences 102, 15545–15550.

Sutherland KD, Song J-Y, Kwon MC, Proost N, Zevenhoven J, and Berns A (2014). Multiple cells-of-origin of mutant K-Ras–induced mouse lung adenocarcinoma. Proceedings of the National Academy of Sciences 111, 4952–4957.

Sweet-Cordero A, Mukherjee S, Subramanian A, You H, Roix JJ, Ladd-Acosta C, Mesirov J, Golub TR, and Jacks T (2005). An oncogenic KRAS2 expression signature identified by cross-species gene-expression analysis. Nature genetics 37, 48. [PubMed: 15608639]

Tammela T, Sanchez-Rivera FJ, Cetinbas NM, Wu K, Joshi NS, Helenius K, Park Y, Azimi R, Kerper NR, and Wesselhoeft RA (2017). A Wnt-producing niche drives proliferative potential and progression in lung adenocarcinoma. Nature 545, 355. [PubMed: 28489818]

Tata PR, and Rajagopal J (2017). Plasticity in the lung: making and breaking cell identity. Development 144, 755–766. [PubMed: 28246210]

Trobridge P, Knoblaugh S, Washington MK, Munoz NM, Tsuchiya KD, Rojas A, Song X, Ulrich CM, Sasazuki T, and Shirasawa S (2009). TGF-β receptor inactivation and mutant Kras induce intestinal neoplasms in mice via a β-catenin-independent pathway. Gastroenterology 136, 1680–1688. e1687. [PubMed: 19208363]

Turner J, Roger J, Fitau J, Combe D, Giddings J, Heeke GV, and Jones CE (2011). Goblet cells are derived from a FOXJ1-expressing progenitor in a human airway epithelium. American journal of respiratory cell and molecular biology 44, 276–284. [PubMed: 20539013]

Uronis JM, Osada T, McCall S, Yang XY, Mantyh C, Morse MA, Lyerly HK, Clary BM, and Hsu DS (2012). Histological and molecular evaluation of patient-derived colorectal cancer explants. PloS one 7, e38422. [PubMed: 22675560]

Vallejo A, Perurena N, Guruceaga E, Mazur PK, Martinez-Canarias S, Zandueta C, Valencia K, Arricibita A, Gwinn D, and Sayles LC (2017). An integrative approach unveils FOSL1 as an oncogene vulnerability in KRAS-driven lung and pancreatic cancer. Nature communications 8, 14294.

van Galen P, Viny AD, Ram O, Ryan RJ, Cotton MJ, Donohue L, Sievers C, Drier Y, Liau BB, and Gillespie SM (2016). A multiplexed system for quantitative comparisons of chromatin landscapes. Molecular cell 61, 170–180. [PubMed: 26687680]

Vierbuchen T, Ling E, Cowley CJ, Couch CH, Wang X, Harmin DA, Roberts CW, and Greenberg ME (2017). AP-1 Transcription Factors and the BAF Complex Mediate Signal-Dependent Enhancer Selection. Molecular cell 68, 1067–1082. e1012. [PubMed: 29272704]

Wang L, Wang E, Prado Balcazar J, Wu Z, Xiang K, Wang Y, Huang Q, Negrete M, Chen KY, and Li W (2021). Chromatin Remodeling of Colorectal Cancer Liver Metastasis is Mediated by an HGF-PU. 1-DPP4 Axis. Advanced Science 8, 2004673.

Winslow MM, Dayton TL, Verhaak RG, Kim-Kiselak C, Snyder EL, Feldser DM, Hubbard DD, DuPage MJ, Whittaker CA, and Hoersch S (2011). Suppression of lung adenocarcinoma progression by Nkx2–1. Nature 473, 101. [PubMed: 21471965]

Wright JR (1990). Clearance and recycling of pulmonary surfactant. American Journal of Physiology-Lung Cellular and Molecular Physiology 259, L1–L12.

Wu J, Huang B, Chen H, Yin Q, Liu Y, Xiang Y, Zhang B, Liu B, Wang Q, and Xia W (2016). The landscape of accessible chromatin in mammalian preimplantation embryos. Nature 534, 652. [PubMed: 27309802]

Wu M, and Gu L (2018). TCseq: Time course sequencing data analysis. R package version 1.

Xi R, Murthy PKL, Tung K-L, Guy CD, Wan J, Li F, Wang Z, Li X, Varanko A, and Rakhilin N (2019). SENP3-mediated host defense response contains HBV replication and restores protein synthesis. PloS one 14, e0209179. [PubMed: 30640896]

Xu X, Huang L, Futtner C, Schwab B, Rampersad RR, Lu Y, Sporn TA, Hogan BL, and Onaitis MW (2014). The cell of origin and subtype of K-Ras-induced lung tumors are modified by Notch and Sox2. Genes & development 28, 1929–1939. [PubMed: 25184679]

Xu X, Rock JR, Lu Y, Futtner C, Schwab B, Guinney J, Hogan BL, and Onaitis MW (2012). Evidence for type II cells as cells of origin of K-Ras–induced distal lung adenocarcinoma. Proceedings of the National Academy of Sciences, 201112499.

Yu T, Chen X, Zhang W, Liu J, Avdiushko R, Napier DL, Liu AX, Neltner JM, Wang C, Cohen D, et al. (2016). KLF4 regulates adult lung tumor-initiating cells and represses K-Ras-mediated lung cancer. Cell Death & Differentiation 23, 207–215.

Zacharias WJ, Frank DB, Zepp JA, Morley MP, Alkhaleel FA, Kong J, Zhou S, Cantu E, and Morrisey EE (2018). Regeneration of the lung alveolus by an evolutionarily conserved epithelial progenitor. Nature 555, 251. [PubMed: 29489752]

Zhang Y, Liu T, Meyer CA, Eeckhoute J, Johnson DS, Bernstein BE, Nusbaum C, Myers RM, Brown M, and Li W (2008). Model-based analysis of ChIP-Seq (MACS). Genome biology 9, R137. [PubMed: 18798982]

Zhu D, Keohavong P, Finkelstein SD, Swalsky P, Bakker A, Weissfeld J, Srivastava S, and Whiteside TL (1997). K-ras gene mutations in normal colorectal tissues from K-ras mutation-positive colorectal cancer patients. Cancer research 57, 2485–2492. [PubMed: 9192830]

Highlights

- AP-1 mediates an epigenome-wide increase in nucleosome occupancy in *Kras*-mutant cells
- FOSL1 based AP-1 recruits mSWI/SNF to displace nucleosomes in *Kras*-mutant cells
- Club or AEC2 cell of origin influences the neoplastic cell state
- Identification of a mutant-*Kras* epigenetic signature conserved across tissues

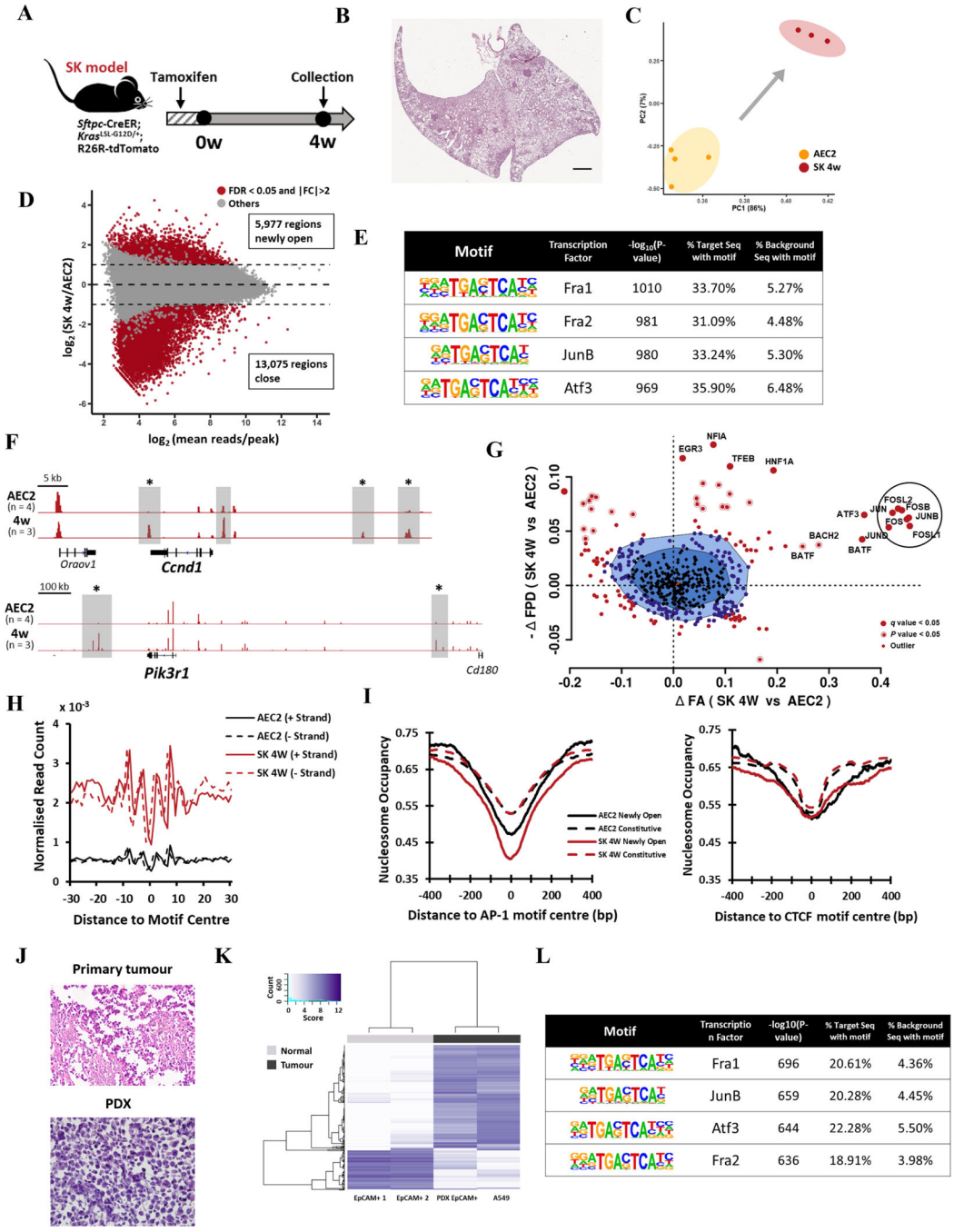

Figure 1. AP-1 mediates epigenome-wide increase in nucleosome occupancy in *Kras*^{G12D} mutant alveolar cells.

A. Schematic showing the experimental design.

B. Representative H&E image of a lung section from a 4w SK mouse. Scale bar represents 1 mm.

C. PCA of ATAC-seq data from AEC2 and SK 4w neoplastic cells.

D. MA-plot showing the differentially accessible chromatin regions in SK 4w and AEC2.

E. TF motifs enriched in the newly open regions in SK 4w neoplastic cells.

F. ATAC-seq signal tracks at *Ccnd1* and *Pik3r1* loci. Newly open regions are shaded. * indicates the presence of AP-1 motif site in the peak.

G. BaGFoot analysis of ATAC-seq data from AEC2 and 4w SK neoplastic cells. AP-1 TFs are circled.

H. Plot showing the normalised ATAC-seq read count of SK 4w and AEC2 cells at the AP-1 motif sites present in differentially accessible regions.

I. Plot showing nucleosome occupancy computed from ATAC-seq of AEC2 and SK 4w neoplastic cells at AP-1 (left) and CTCF (right) motif sites in constitutive and newly open peaks.

J. Representative H&E images of the primary human lung adenocarcinoma and the PDX generated from it. Both the primary and PDX tumour cells consist of sheets and nests of large, pleomorphic neoplastic epithelial cells devoid of glandular or squamous differentiation. Scale bar represents 50 μm.

K. Heatmap showing differentially accessible regions on the chromatin of normal human pulmonary epithelial cells and lung adenocarcinoma cells.

L. TF motifs enriched in the newly open regions (with $\log_2$ FC > 4) in human lung adenocarcinoma.

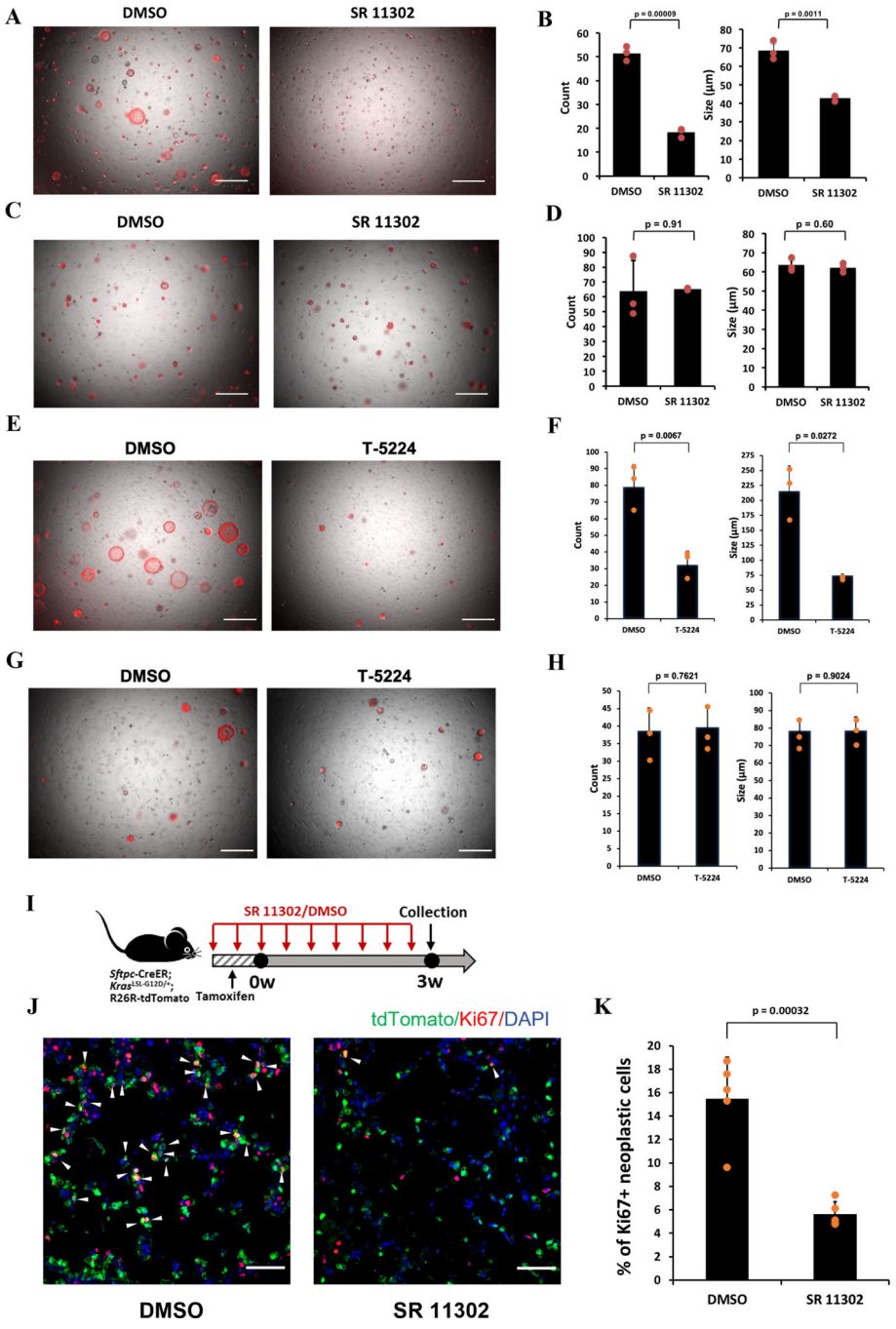

Figure 2. Pharmacological inhibition of AP-1 reduces proliferation of *Kras*-mutant AEC2 cells *in vitro* and *in vivo*.

(A-B) Normal AEC2 cells from SK mice were plated in matrigel containing 4-OHT to induce $Kras^{G12D}$ expression for 24 hours. They were also treated with AP-1 inhibitor SR 11302 or DMSO (vehicle control) and colony (spheroid) formation ability of the cells was assayed after 8 days.

A. Representative IF images showing the sphere formation ability. Scale bar represents 500 μm.

B. Quantification of spheroid size and number (n=3 independent experiments).

(C-D) Normal AEC2 cells from *Sftpc*-CreER; R26R-tdTomato mice were plated in matrigel. They were treated with AP-1 inhibitor SR 11302 or DMSO (vehicle control) and colony (spheroid) formation ability of the cells was assayed after 8 days.

C. Representative IF images showing the sphere formation ability. Scale bar represents 500 μm.

D. Quantification of spheroid size and number (n=3 independent experiments).

(E-F) Normal AEC2 cells from SK mice were plated in matrigel containing 4-OHT to induce $Kras^{G12D}$ expression for 24 hours. They were also treated with AP-1 inhibitor T-5224 or DMSO (vehicle control) and colony (spheroid) formation ability of the cells was assayed after 8 days.

E. Representative IF images showing the sphere formation ability. Scale bar represents 500 μm.

F. Quantification of spheroid size and number (n=3 independent experiments).

(G-H) Normal AEC2 cells from *Sftpc*-CreER; R26R-tdTomato mice were plated in matrigel. They were treated with AP-1 inhibitor T-5224 or DMSO (vehicle control) and colony (spheroid) formation ability of the cells was assayed after 8 days.

G. Representative IF images showing the sphere formation ability. Scale bar represents 500 μm.

H. Quantification of spheroid size and number (n=3 independent experiments).

I. Schematic showing the experimental design.

J. Representative IF images showing Ki67 in red and tdTomato in green in mice treated with DMSO or SR 11302. DAPI in blue labels nuclei and scale bar represents 50 μm.

K. The bar plot shows the percent of $Ki67^{+}$ cells among the lineage labelled population in SR 11302 and DMSO treated mice (n=5 mice/condition).

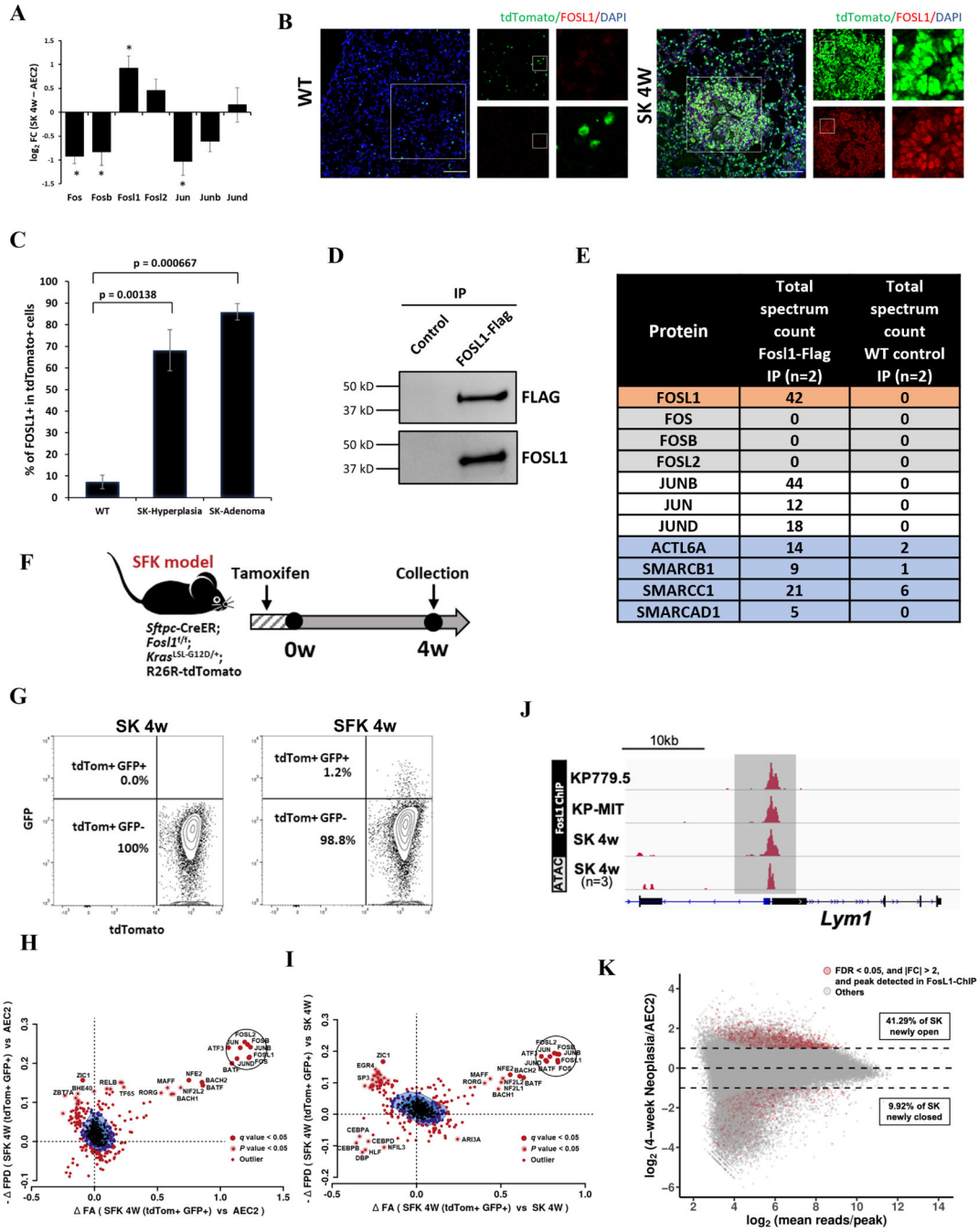

Protein	Total spectrum count Fosl1-Flag IP (n=2)	Total spectrum count WT control IP (n=2)
FOSL1	42	0
FOS	0	0
FOSB	0	0
FOSL2	0	0
JUNB	44	0
JUN	12	0
JUND	18	0
ACTL6A	14	2
SMARCB1	9	1
SMARCC1	21	6
SMARCAD1	5	0

Figure 3. FOSL1 based AP-1 complex recruits mSWI/SNF to displace nucleosomes in *Kras*-mutant cells.

A. Bar plot summarising the changes to expression levels of AP-1 genes in the SK model as detected by RNA-seq. * indicates statistical significance (q value < 0.05 and |FC| > 1.5).

B. Representative IF images showing the expression of *Fosl1* (red) and tdTomato (green) in SC (WT) and SK 4w lungs. DAPI (blue) shows nuclei and the scale bar represents 100 μm. Zoomed-in single-channel images are shown for the regions highlighted by inset-squares.

C. Quantification of FOSL1^{+} lineage-labelled cells from Fig. 3B (n=3 mice/condition).

(D-E) FOSL1 was immunoprecipitated from A549-Fosl1-Flag cell line. A549 WT was used as control.

D. Representative Western Blot images showing the detection of Flag tag and FOSL1 protein.

E. AP-1 and mSWI/SNF complex proteins co-immunoprecipitated with FOSL1 as identified by MS.

F. Schematic showing the experimental design.

G. (right) FACS gating used to isolate GFP+ population among lineage labelled (tdTomato+) cells from SFK mice at 4 weeks post Cre induction. (left) SK 4w neoplastic cells were used as a negative control.

H. BaGFoot analysis of ATAC-seq data from AEC2 and SFK 4w neoplastic cells ($tdTom^+$ GFP^+). AP-1 transcription factors are circled.

I. BaGFoot analysis of ATAC-seq data from SK 4w neoplastic cells and SFK 4w neoplastic cells ($tdTom^+$ GFP^+). AP-1 transcription factors are circled.

J. FOSL1 ChIP-seq tracks at *Lym1* locus. ATAC-seq signal track is shown for reference. Common peak has been shaded.

K. FOSL1 binding sites, identified by ChIP-seq, in differentially accessible regions are shown in red in the MA-plot from Fig. 1D.

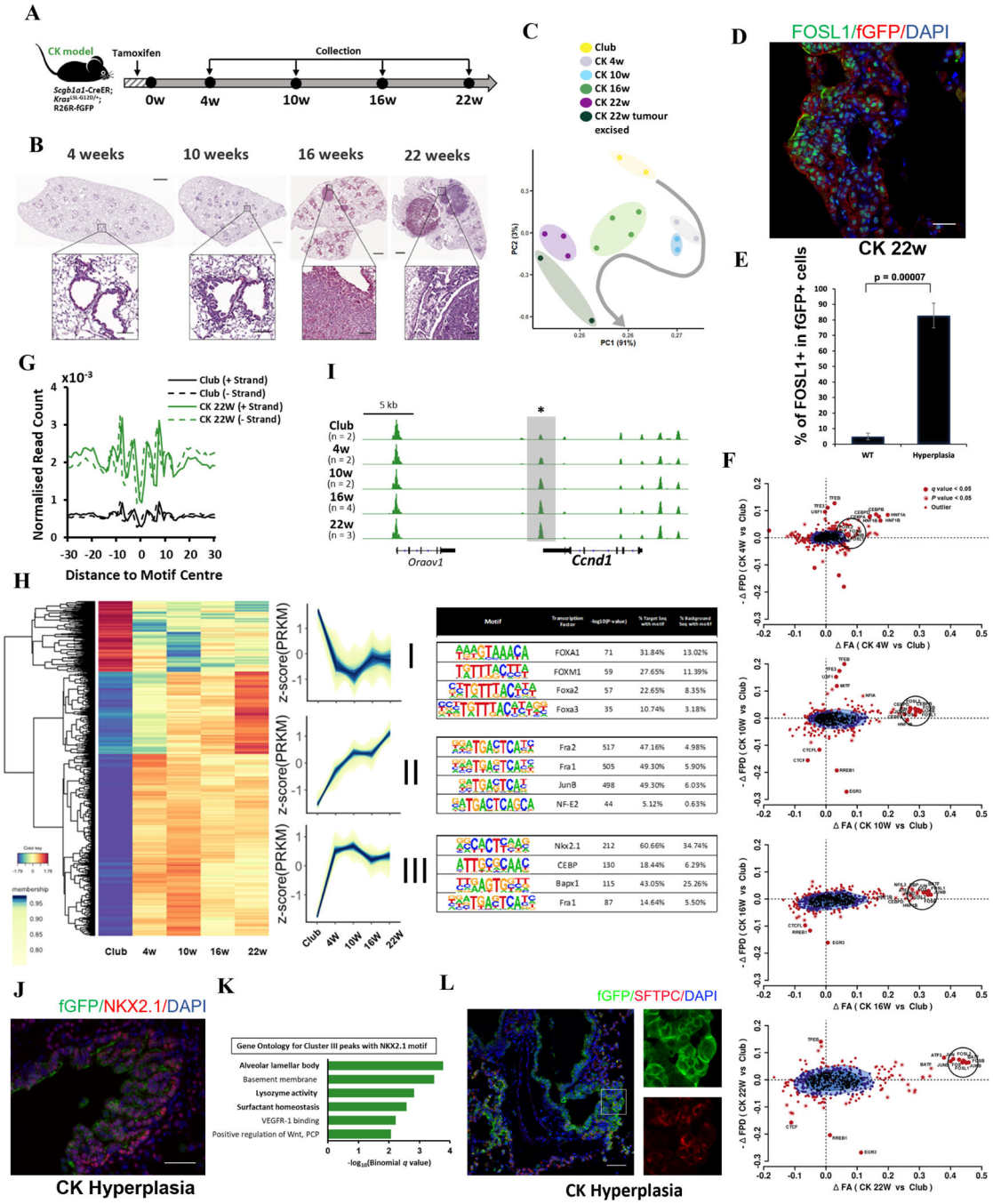

Figure 4. De-multiplexing cellular plasticity and proliferative signal in club cell origin tumours.

A. Schematic showing the experimental design.

B. Representative H&E images of lung sections from CK mice at 4, 10, 16 and 22 weeks after tamoxifen doses. Scale bar represents 1 mm (whole-lobe images) and 100 μm (zoomed-in regions).

C. PCA of ATAC-seq data from normal club cells and neoplastic cells from CK (4w, 10w, 16w and 22w) mouse lungs. Arrow indicates tumour progression.

D. Representative IF image showing the expression of FOSL1 (green) and fGFP (red) in CK 22w lungs. DAPI (blue) shows nuclei and the scale bar represents 25 μm.

E. Quantification of $FOSL1^+$ lineage-labelled cells from Fig. 4D (n=3 mice/condition).

F. BaGFoot analysis of ATAC-seq data from club and CK neoplastic cells. AP-1 transcription factors are circled.

G. Plot showing the normalised ATAC-seq read count of CK 22w and club cells at the AP-1 motif sites present in differentially accessible regions.

H. Heatmap shows the differentially accessible regions on the chromatin of club and CK neoplastic cells. Hierarchical clustering of these regions yields three groups with distinct temporal dynamics. The tables on the right show the top enriched TF motifs found in the respective cluster.

I. ATAC-seq signal tracks at the *Ccnd1* locus. Newly open region is shaded. * indicates the presence of AP-1 motif site in the peak.

J. Representative IF image showing the expression of NKX2.1 (red) and fGFP (green) in CK 22w hyperplastic regions. DAPI (blue) shows nuclei and the scale bar represents 50 μm.

K. Gene Ontology terms, obtained from GREAT analysis, for the peaks in Cluster III (Figure 4H) harbouring an NKX2.1 motif.

L. Representative image showing the expression of SPC (red) and fGFP (green) cells in CK 4w hyperplastic cells. DAPI, shown in blue, labels the nuclei and the scale represents 50 μm. Zoomed-in single-channel images are shown for the regions highlighted in the inset.

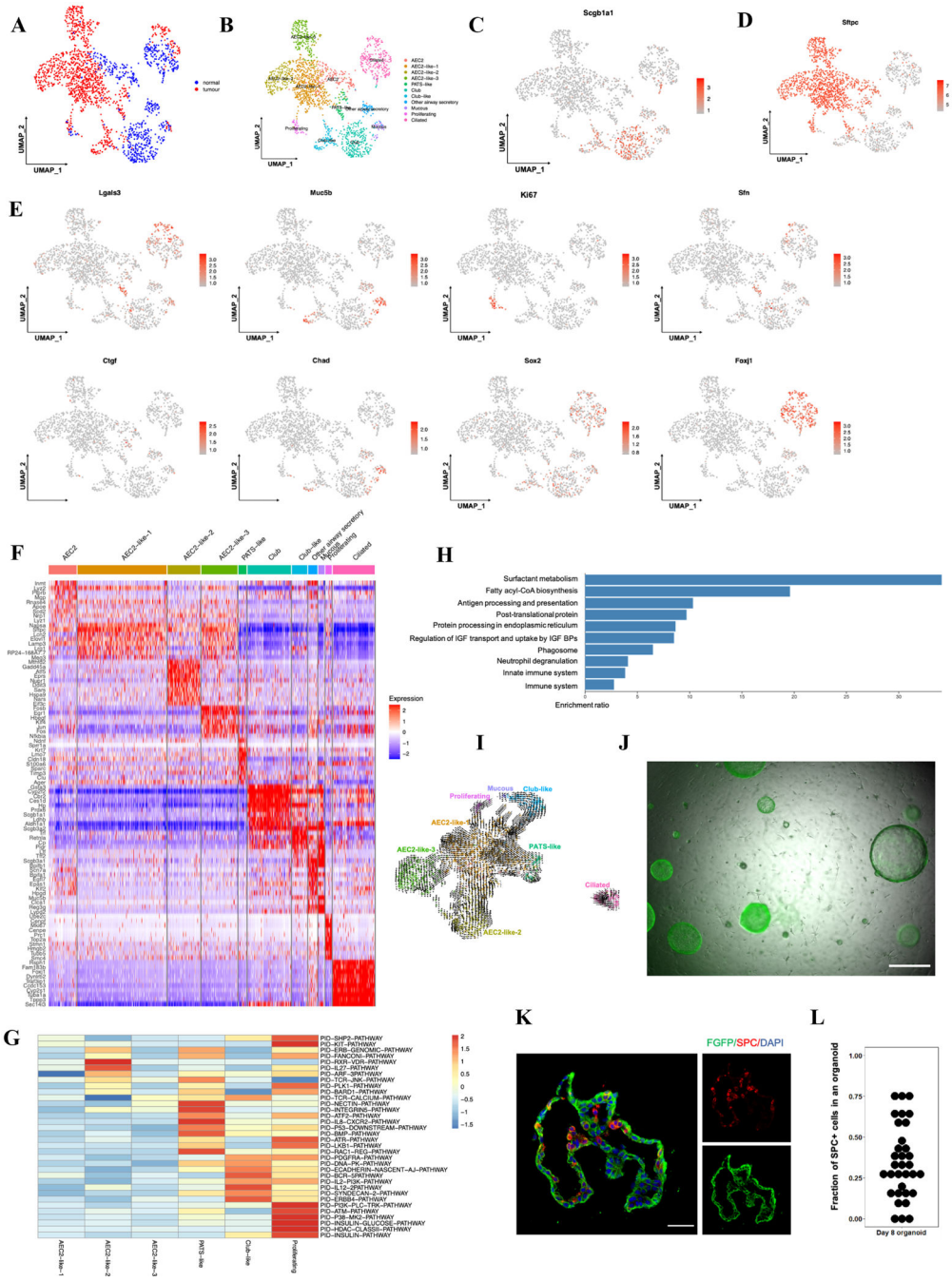

Figure 5. Analysis of CK tumours at single-cell resolution.

A. UMAP visualisation of normal epithelial and neoplastic cells from CC and CK models.

B. UMAP showing various cell-types identified by scRNA-seq.

C. UMAP showing the expression of *Scgb1a1*.

D. UMAP showing the expression of *Sftpc*.

E. UMAP plots showing the expression of indicated genes.

F. Heatmap showing the expression of differentially expressed genes in normal epithelial and neoplastic cell-types.

G. Heatmap showing pathways enriched in neoplastic cell clusters.

H. Bar-plot showing the pathways upregulated in club-like neoplastic cells when compared to normal club cells.

I. RNA velocity analysis showing cellular trajectories in CK neoplastic cell populations.

(J-L) Four doses of tamoxifen were injected to CK mice and lungs were harvested after 2 days. Lysotracker^{-} fGFP^{+} cells were isolated by FACS and plated with MRC5 fibroblasts in matrigel. The cells were cultured for ten days before fixation.

J. Representative IF image showing the organoids. fGFP is shown in green, brightfield in grey and scale bar represents 200 μm.

K. Representative IF image showing the expression of SFTPC (red) and fGFP (green). DAPI (blue) shows nuclei and the scale bar represents 50 μm.

L. Quantification showing the fraction of SPC^{+} cells in an organoid from Fig. 5K (n= 3 independent experiments).

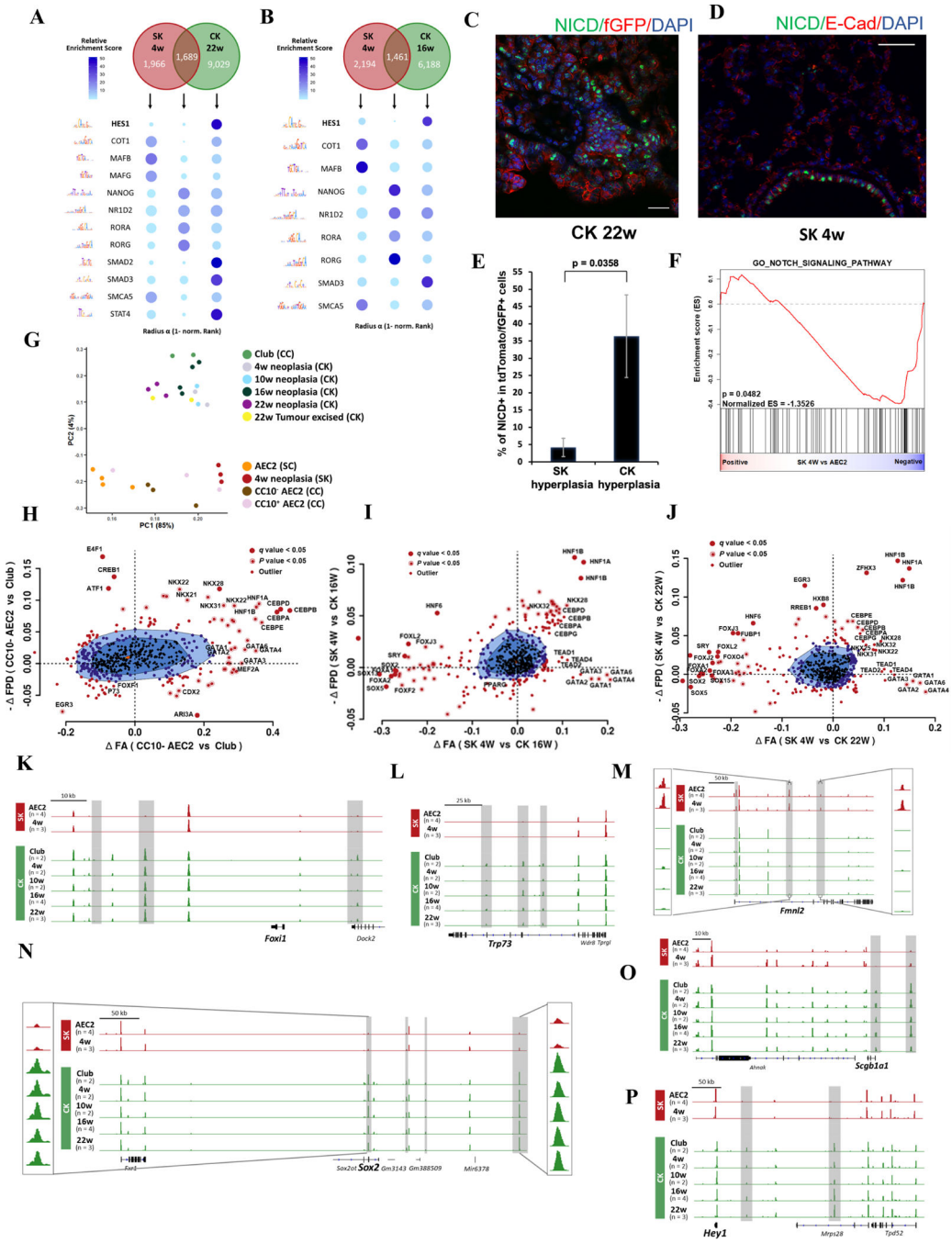

Figure 6. Cell of origin influences the neoplastic cell state.

A. (top) Venn diagram showing the number of overlapping newly open regions that harbour an AP-1 motif in SK 4w and CK 22w neoplastic cells. (bottom) Bubble plot showing the top enriched motifs in the neighbourhood of putative AP-1 binding sites.

B. (top) Venn diagram showing the number of overlapping newly open regions that harbour an AP-1 motif in SK 4w and CK 16w neoplastic cells. (bottom) Bubble plot showing the top enriched motifs in the neighbourhood of putative AP-1 binding sites.

C. Representative IF image showing the level of NICD (green) in CK 22w lungs. Lineage label fGFP is shown in red and DAPI (blue) represents nuclei. Scale bar represents 25 μm.
D. Representative IF image showing the level of NICD (green) in SK 4w lungs. E-cadherin is shown in red and DAPI (blue) represents nuclei. Scale bar represents 50 μm.
E. Quantification of $NICD^+$ cells in hyperplastic regions of SK 4w and CK (16w and 22w) lungs from Fig. 6B–C (n=3 mice/condition).
F. GSEA of RNA-seq data shows that Notch activity has reduced in SK 4w neoplastic cells when compared to AEC2.
G. PCA of ATAC-seq data from normal and neoplastic cells collected from SC (AEC2), CC (Club, $CC10^+$ AEC2 and $CC10^-$ AEC2), SK (4w) and CK (4w, 10w, 16w, 22w and 22w tumour-excised) mouse lungs.
H. BaGFoot analysis of ATAC-seq data from CC10− AEC2 and Club cells.
I. BaGFoot analysis of ATAC-seq data from SK 4w and CK 16w neoplastic cells.
J. BaGFoot analysis of ATAC-seq data from SK 4w and CK 22w neoplastic cells.
(K-P) ATAC-seq signal tracks at *Foxi1* (K), *Trp73* (L), *Fmnl2* (M), *Sox2* (N), *Scgb1a1* (O) and *Hey1* (P) loci.

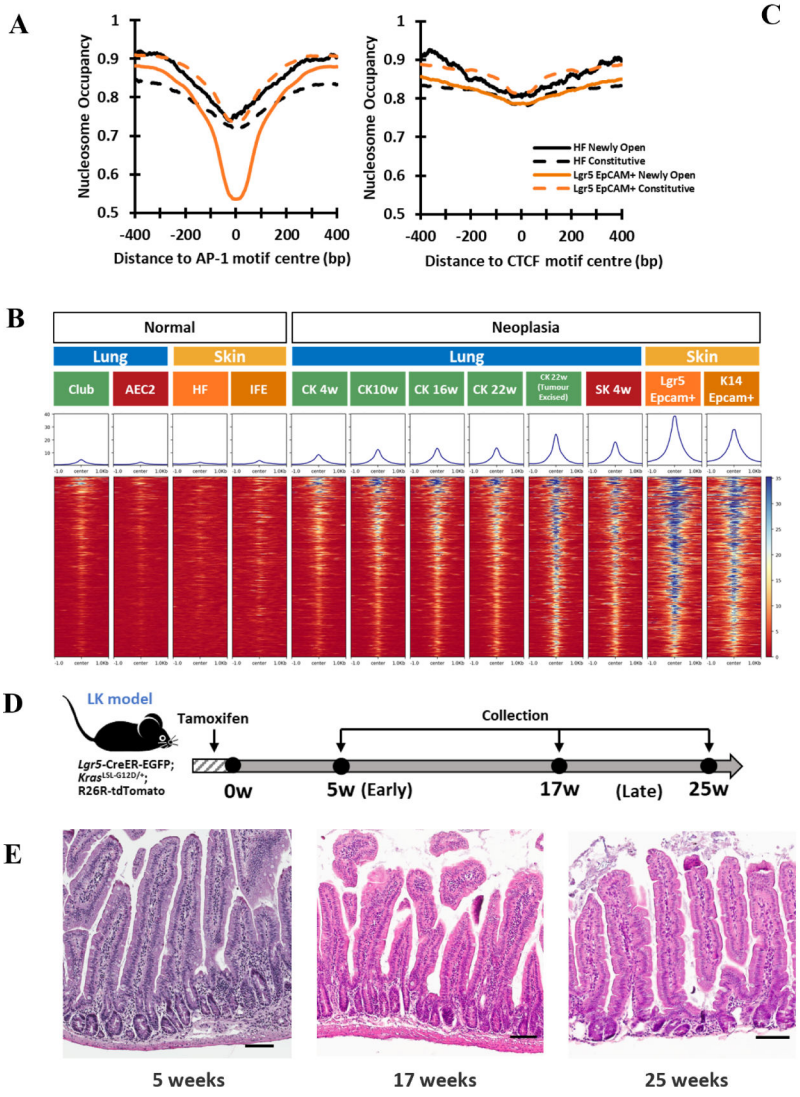

C

Ontology Term	-log10 (Binomial q value)
Gene promoters occupied by SMAD2/3 in HaCaT cells	6.92
Genes up-regulated in papillary thyroid carcinoma	5.85
Genes up-regulated in intestinal crypt cells upon deletion of CTNNB1	4.53
Validated transcriptional targets of Fra1 and Fra2	4.17
Cell Cycle: G1/S Check Point	2.88
p53 pathway	1.47

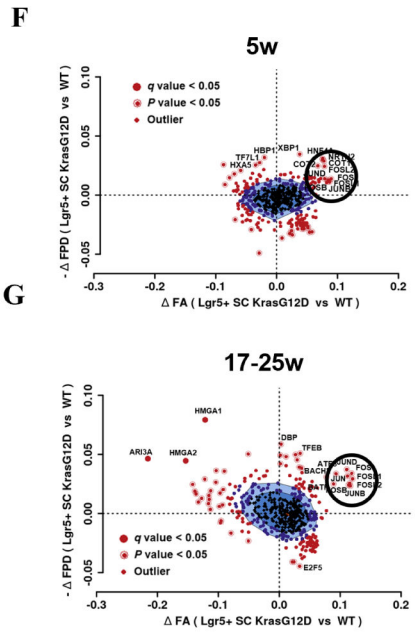

Figure 7. Identification of a mutant-*Kras* epigenetic signature conserved across tissues.

A. Plot showing nucleosome occupancy computed from ATAC-seq of HF stem cells and neoplastic cells derived from them (*Lgr5* EpCAM$^+$) at AP-1 (left) and CTCF (right) motif sites in constitutive and newly open peaks. Data from (Latil et al., 2017).

B. ATAC-seq heatmap showing conserved regions with increased accessibility in *Kras*-mutant neoplastic cells derived from AEC2, club, HF stem and intra-follicular epidermal stem cells, and harbouring an AP-1 motif.

C. GREAT analysis of the regions shown in Figure 7B.

D. Schematic showing the experimental design.

E. Representative H&E images of intestinal sections from LK mice. Scale bar represents 100 μm.

F. BaGFoot analysis of ATAC-seq data from early stage (5w) *Kras* mutant and WT *Lgr5*$^+$ stem cells. AP-1 transcription factors are circled.

G. BaGFoot analysis of ATAC-seq data from late stage (17–25w) *Kras* mutant and WT *Lgr5*+ stem cells. AP-1 transcription factors are circled.

KEY RESOURCES TABLE

REAGENT or RESOURCE	SOURCE	IDENTIFIER
Antibodies		
Monoclonal ANTI-FLAG® M2 antibody produced in mouse	Sigma-Aldrich	Cat #: F1804 RRID: AB_262044
Anti-Ki67 antibody	Abcam	Cat #: ab15580 RRID: AB_443209
Ki-67 (D3B5) Rabbit mAb (Mouse Preferred; IHC Formulated)	Cell Signaling Technology	Cat #: 12202 RRID: AB_2620142
β-Actin (13E5) Rabbit mAb	Cell Signaling Technology	Cat #: 4970 RRID: AB_2223172
Cleaved Notch1 (Val1744) (D3B8) Rabbit mAb	Cell Signaling Technology	Cat #: 4147 RRID: AB_2153348
Anti-GFP antibody	Abcam	Cat #: ab13970 RRID: AB_300798
Anti-GFP antibody	Abcam	Cat #: ab5450 RRID: AB_304897
Anti-GFP antibody - ChIP Grade	Abcam	Cat #: ab290 RRID: AB_303395
tdTomato antibody	Sicgen	Cat #: AB8181-200 RRID: AB_2722750
Anti-Fra-1 Antibody (D-3)	Santa Cruz Biotechnology	Cat #: sc-376148 RRID: AB_11012022
Anti-Fra-1 Antibody (C-12)	Santa Cruz Biotechnology	Cat #: sc-28310 RRID: AB_627632
Anti-Fra-1 Antibody	Abcam	Cat #: ab252421
Anti-Nkx2.1 antibody	Abcam	Cat #: sc-13040 RRID: AB_793532
Anti-E-Cadherin antibody	Abcam	Cat #: 76055 RRID: AB_1310159
APC anti-human CD326 (EpCAM) Antibody	Biolegend	Cat #: 324207 RRID: AB_756081
Bacterial and Virus Strains		
E. coli: DH5α Competent Cells	Thermo Fisher Scientific	Cat #: 18258012
Chemicals, Peptides, and Recombinant Proteins		
Tamoxifen	Sigma-Aldrich	Cat #: T5648-1G
SR 11302	Tocris	Cat #: 2476
SR 11302	Santa Cruz Biotechnology	Cat #: sc-204295
T-5224	Cayman Chemical	Cat #: 22904
Cholera Toxin from *Vibrio cholerae*	Sigma-Aldrich	Cat #: C8052-.5MG
Bovine Pituitary Extract (BPE)	Thermo Fisher Scientific	Cat #: 13028014
Insulin-Transferrin-Selenium-Sodium Pyruvate (ITS-A) (100X)	Thermo Fisher Scientific	Cat #: 51300044
Recombinant Mouse EGF Protein, CF	R&D Systems	Cat #: 2028-EG-200
Retinoic acid	Sigma-Aldrich	Cat #: R2625-50MG
3X FLAG Peptide	Sigma-Aldrich	Cat #: F4799-4MG
(Z)-4-Hydroxytamoxifen	Sigma-Aldrich	Cat #: H7904-5MG

REAGENT or RESOURCE	SOURCE	IDENTIFIER
SYTOX Blue Dead Cell Stain, for flow cytometry	Thermo Fisher Scientific	Cat #: S34857
LysoTracker Red DND-99	Thermo Fisher Scientific	Cat #: L7528
LysoTracker Green DND-26	Thermo Fisher Scientific	Cat #: L7526
ACCUMAX	STEMCELL Technologies	Cat #: 07921
Y-27632	STEMCELL Technologies	Cat #: 72304
ACK Lysing Buffer	Thermo Fisher Scientific	Cat #: A1049201
RT-PCR Grade Water	Thermo Fisher Scientific	Cat #: AM9935
SYBR™ Green I Nucleic Acid Gel Stain - 10,000X concentrate in DMSO	Thermo Fisher Scientific	Cat #: S7563
RNase-Free DNase Set	Qiagen	Cat #: 79254
Ham's F-12K (Kaighn's) Medium	Thermo Fisher Scientific	Cat #: 21127030
DMEM/F-12, HEPES	Thermo Fisher Scientific	Cat #: 11330057
Halt Protease and Phosphatase Inhibitor Single-Use Cocktail (100X)	Thermo Fisher Scientific	Cat #: 78442
Corn oil (delivery vehicle for fat-soluble compounds)	Sigma-Aldrich	Cat #: C8267-500ML
Cas9 protein with NLS, high concentration	PNA Bio	Cat #: CP02
Paraformaldehyde	Sigma-Aldrich	Cat #: P6148-500G
Matrigel Growth Factor Reduced (GFR) Basement Membrane Matrix	Corning	Cat #: 354230
MEM (Minimum Essential Medium)	Thermo Fisher Scientific	Cat #: 11095098
Proteinase K	Thermo Fisher Scientific	Cat #: 26160
MNAse	New England BioLabs	Cat #: M0247S
TrueBlack Lipofuscin Autofluorescence Quencher	Biotium	Cat #: 23007
VECTASHIELD Antifade Mounting Medium with DAPI	Vector Laboratories	Cat #: H-1200
DAKO Protein Block, Serum-Free	Agilent	Cat #: X090930-2
Perfluorooctanol (PFO), 97%	Sigma	Cat #: 370533-25G
Klenow Fragment (3'→5' exo-)	New England BioLabs	Cat #: M0212L
Exonuclease I	New England BioLabs	Cat #: M0293L
Maxima H Minus Reverse Transcriptase	Thermo Fisher Scientific	Cat #: EP0753
Critical Commercial Assays		
Nextera DNA Library Prep Kit	Illumina	Cat #: FC-121-1030
NEBNext High-Fidelity 2X PCR Master Mix	New England BioLabs	Cat #: M0541S
Nextera XT DNA Library Preparation Kit	Illumina	Cat #: FC-131-1096
MinElute PCR Purification Kit	Qiagen	Cat #: 28006
QIAquick PCR Purification Kit	Qiagen	Cat #: 28106
RNeasy Mini Kit	Qiagen	Cat #: 74104
QuantiFast SYBR Green PCR Kit	Qiagen	Cat #: 204054
QuantiTect Reverse Transcription Kit	Qiagen	Cat #: 205310
Tumor Dissociation Kit, mouse	Miltenyi Biotec	Cat #: 130-096-730
Lung Dissociation Kit, mouse	Miltenyi Biotec	Cat #: 130-095-927
Tumor Dissociation Kit, human	Miltenyi Biotec	Cat #: 130-095-929

REAGENT or RESOURCE	SOURCE	IDENTIFIER
CD45 MicroBeads, mouse	Miltenyi Biotec	Cat #: 130-052-301
CD45 MicroBeads, human	Miltenyi Biotec	Cat #: 130-045-801
Anti-FLAG M2 Magnetic Beads	Sigma-Aldrich	Cat #: M8823-1ML
Phusion Hot Start II High-Fidelity PCR Master Mix	Thermo Fisher Scientific	Cat #: F565S
MEGAshortscript™ T7 Transcription Kit	Thermo Fisher Scientific	Cat #: AM1354
MEGAclear™ Transcription Clean-Up Kit	Thermo Fisher Scientific	Cat #: AM1908
Terra™ PCR Direct Polymerase Mix	Takara	Cat #: 639271
Dynabeads™ MyOne™ Silane	Thermo Fisher Scientific	Cat #: 37002D
Pierce™ ChIP-grade Protein A/G Magnetic Beads	Thermo Fisher Scientific	Cat #: 26162
HiScribe T7 Quick High Yield RNA Synthesis kit	New England BioLabs	Cat #: E2050S
Fast-Link DNA Ligation kit	Lucigen	Cat #: LK6201H
End-It DNA End-Repair kit	Lucigen	Cat #: ER81050
SuperScript III First-Strand Synthesis SuperMix	Thermo Fisher Scientific	Cat #: 18080-400
TSA Plus Fluorescein Evaluation Kit	PerkinElmer	Cat #: NEL741E001KT
Deposited Data		
ATAC-seq of normal and neoplastic lung epithelial cells	This paper	GEO: GSE183873
RNA-seq of normal and neoplastic lung epithelial cells	This paper	GEO: GSE183874
scRNA-seq of normal and neoplastic lung epithelial cells	This paper	GEO: GSE183875
FOSL1 Mint-ChIP on neoplastic lung epithelial cells	This paper	GEO: GSE192406
FOSL1 IP followed by mass spectrometry proteomics datasets	This paper	ProteomeXchange: PXD030574 https://doi.org/doi:10.25345/C5BG5B
Uncropped western blot images	This paper	Mendeley data https://data.mendeley.com/ Reserved DOI: 10.17632/mtrfthzdd3.1
ATAC-seq of normal and neoplastic skin cells	(Latil et al., 2017)	GEO: GSE88989
ATAC-seq of A549 cells	(Consortium, 2012)	GEO: GSE114202
ATAC-seq of normal colon organoids	(Devall et al., 2020)	NCBI BioProject: PRJNA596536
ATAC-seq of colon cancer cell-line	(Allen et al., 2019)	GEO: GSE113219
ATAC-seq of colon cancer cell lines	(Wang et al., 2021)	GEO: GSE153016
Experimental Models: Cell Lines		
Human: MRC-5 cells	Duke University Cell Culture Facility (Duke CCF)	N/A
Human: A549 cells (FOSL1-FLAG)	(Seo et al., 2021)	N/A
Human: A549 cells	ATCC	CCL-185
Mouse: KP cells	(Dimitrova et al., 2016)	N/A
Mouse: KP cells	(Vallejo et al., 2017)	N/A
Experimental Models: Organisms/Strains		
Mouse: *Sftpc*-CreER^{T2}	(Xu et al., 2012)	N/A
Mouse: *Scgb1a1*-CreER™	(Rawlins et al., 2009)	N/A
Mouse: *Rosa26R*-tdTomato	(Xu et al., 2012)	N/A
Mouse: *Kras*$^{LSL-G12D/+}$	(Xu et al., 2012)	N/A

REAGENT or RESOURCE	SOURCE	IDENTIFIER
Mouse: *Rosa26R*-fGFP	(Xu et al., 2012)	N/A
Mouse: *Fosl1*$^{fl/fl}$	(Eferl et al., 2004)	N/A
Mouse: *Lgr5*-EGFP-IRES-creERT2	The Jackson Laboratory	JAX #: 008875
Mouse: NOD.CB17-Prkdcscid/J	The Jackson Laboratory	JAX #: 001303
Oligonucleotides		
qPCR Primer for *Sftpc* (NM_011359.2)	GeneCopoeia	Cat #: MQP094943
qPCR Primer for *Scgb1a1* (NM_011681.2)	GeneCopoeia	Cat #: MQP030442
qPCR Primer for *Actb* (NM_007393.5)	GeneCopoeia	Cat #: MQP026493
qPCR Primer for *Fosl1* (NM_010235.2)	GeneCopoeia	Cat #: MQP029189
Recombinant DNA		
Mouse gRNA pooled sub-library targeting mitochondrial DNA (pUC57kan-T7-mt-gRNA)	(Wu et al., 2016)	Addgene (Pooled Library #82480)
Software and Algorithms		
GREAT	(McLean et al., 2010)	http://great.stanford.edu/public/html/
EdgeR	(Robinson et al., 2010)	https://bioconductor.org/packages/release/bioc/html/edgeR.html
MACS	(Zhang et al., 2008)	https://github.com/taoliu/MACS
featureCounts	(Liao et al., 2014)	https://bioinf.wehi.edu.au/featureCounts/
TCseq	(Wu and Gu, 2018)	https://bioconductor.org/packages/release/bioc/html/TCseq.html
Diffbind	(Stark and Brown, 2011)	https://bioconductor.org/packages/release/bioc/html/DiffBind.html
Homer	(Heinz et al., 2010)	https://homer.ucsd.edu/homer/
BaGFoot	(Baek et al., 2017)	N/A
FIMO	(Bailey et al., 2009)	https://meme-suite.org/index.html
Centrimo	(Bailey et al., 2009)	https://meme-suite.org/index.html
NucleoATAC	(Schep et al., 2015)	https://nucleoatac.readthedocs.io/en/latest/
Fiji	(Schindelin et al., 2012)	https://imagej.net/Fiji
Aperio Imagescope	N/A	https://www.leicabiosystems.com/digital-pathology/manage/aperio-imagescope/
DeepTools	(Ramírez et al., 2014)	https://deeptools.readthedocs.io/en/develop/
BEDTools	(Quinlan and Hall, 2010)	https://bedtools.readthedocs.io/en/latest/
SAMTools	(Li et al., 2009)	https://www.htslib.org/doc/samtools.html
mixOmics	(Rohart et al., 2017)	https://mixomics.org
Bowtie 2	(Langmead and Salzberg, 2012)	N/A
PIQ	(Sherwood et al., 2014b)	N/A
Seurat	(Stuart et al., 2019)	https://satijalab.org/seurat/
STAR	(Dobin et al., 2013)	N/A
rtracklayer	(Lawrence et al., 2009)	https://bioconductor.org/packages/release/bioc/html/rtracklayer.html
GenomicRanges	(Lawrence et al., 2013)	https://bioconductor.org/packages/release/bioc/html/GenomicRanges.html

REAGENT or RESOURCE	SOURCE	IDENTIFIER
Mint-ChIP	N/A	https://github.com/jianhong/MintChIP
dropSeqPipe	N/A	https://hoohm.github.io/dropSeqPipe/